



HAL
open science

Mars water vapor abundance from SPICAM IR spectrometer: Seasonal and geographic distributions

Anna Fedorova, Oleg Korablev, Jean-Loup Bertaux, Alexander Rodin,
Alexander Kiselev, Severine Perrier

► To cite this version:

Anna Fedorova, Oleg Korablev, Jean-Loup Bertaux, Alexander Rodin, Alexander Kiselev, et al.. Mars water vapor abundance from SPICAM IR spectrometer: Seasonal and geographic distributions. Journal of Geophysical Research. Planets, 2006, 111, pp.E09S08. 10.1029/2006JE002695 . hal-00101137

HAL Id: hal-00101137

<https://hal.science/hal-00101137>

Submitted on 12 Jan 2021

HAL is a multi-disciplinary open access archive for the deposit and dissemination of scientific research documents, whether they are published or not. The documents may come from teaching and research institutions in France or abroad, or from public or private research centers.

L'archive ouverte pluridisciplinaire **HAL**, est destinée au dépôt et à la diffusion de documents scientifiques de niveau recherche, publiés ou non, émanant des établissements d'enseignement et de recherche français ou étrangers, des laboratoires publics ou privés.

Mars water vapor abundance from SPICAM IR spectrometer: Seasonal and geographic distributions

Anna Fedorova,¹ Oleg Korablev,¹ Jean-Loup Bertaux,² Alexander Rodin,^{1,3} Alexander Kiselev,¹ and Severine Perrier²

Received 2 February 2006; revised 7 July 2006; accepted 11 July 2006; published 26 September 2006.

[1] The near-IR channel of SPICAM experiment on Mars Express spacecraft is a 800-g acousto-optic tunable filter (AOTF)–based spectrometer operating in the spectral range of 1–1.7 μm with resolving power of ~ 2000 . It was put aboard as an auxiliary channel dedicated to nadir H_2O measurements in the 1.37- μm spectral band. This primary scientific goal of the experiment is achieved through successful water vapor retrievals, resulting in spatial and seasonal distributions of H_2O . We present the results of H_2O retrieval from January 2004 ($L_s = 330^\circ$) to December 2005 ($L_s = 340^\circ$), covering the entire Martian year. The seasonal trend of water vapor obtained by SPICAM IR is consistent with TES results and reveals disagreement with MAWD results related to south pole maximum. The main feature of SPICAM measurements is globally smaller water vapor abundance for all seasons and locations including polar regions, as compared to other data. The maximum abundance is 50–55 precipitable microns at the north pole and 13–16 precipitable microns (pr μm) at the south pole. The northern tropical maximum amounts to 12–15 pr μm . Possible reasons for the disagreements are discussed.

Citation: Fedorova, A., O. Korablev, J.-L. Bertaux, A. Rodin, A. Kiselev, and S. Perrier (2006), Mars water vapor abundance from SPICAM IR spectrometer: Seasonal and geographic distributions, *J. Geophys. Res.*, *111*, E09S08, doi:10.1029/2006JE002695.

1. Introduction

[2] Although water vapor is a minor constituent of the Martian atmosphere (just several precipitable microns in atmospheric column) it plays a major role in Mars climate. It is a condensable specie actively interacting with surface and it varies in several times during the Martian year. Systematic monitoring of water vapor and comparison with Martian general circulation models (MGCMS) helps to understand main processes controlling the distribution of water vapor, such as seasonal changes in solar energy, exchange with the surface, and cloud formation [Montmessin *et al.*, 2004]. Such understanding could provide insights into the history of Mars climate, and to contribute to the question about “wet” early Mars. For example, hydrogen-rich regions at Mars equator discovered by Mars Odyssey [Feldman *et al.*, 2004; Mitrofanov *et al.*, 2002] could be explained as a result of atmospheric water transport and accumulation [Feldman *et al.*, 2005; Basilevsky *et al.*, 2006].

[3] After the first detection of water by Spinrad *et al.* [1963] in 8200 \AA H_2O absorption band there have been numerous ground-based observations of Martian water in the near-IR band [Barker *et al.*, 1970; Barker, 1976]. These

episodic observations could not quantify the seasonal cycle of water. Only recently a large series of near-infrared measurements characterized the seasonal distribution of H_2O from the ground [Rizk *et al.*, 1991; Sprague *et al.*, 1996, 2001, 2003, 2006].

[4] Martian atmospheric water has been extensively measured by landers and orbiters in the past. First seasonal variations of H_2O in the polar regions of Mars were observed by Mariner 9 IR spectrometer [Conrath *et al.*, 1973]. The first mapping of the water vapor with a complete seasonal coverage has been obtained in the 1.38 μm absorption band by the Martian Atmospheric Water Detector (MAWD) on Viking 1 and 2 orbiters [Farmer and LaPorte, 1972; Farmer *et al.*, 1977; Jakosky and Farmer, 1982]. The MAWD data set covers more than one Martian year from June 1976 through April 1979. This observation have shown large spatial and temporal variations of the water column density with a maximum around 80–100 precipitable microns (pr μm) in summer north pole. For a long time these data have been a classical framework constraining the Martian water cycle models. The southern hemisphere summer the MAWD data was very dry according to the MAWD data, i.e., about 5–10 pr μm . At that time two global dust storms have occurred near the perihelion (areocentric longitude of Sun $L_s \sim 205^\circ$ and $\sim 275^\circ$), and many authors have suggested that the near IR measurements by MAWD could be affected by dust scattering [Davies, 1979; Davies and Wainio, 1981; Jakosky *et al.*, 1988]. The influence of dust was addressed by Fedorova *et al.* [2004]; the retrieved H_2O were corrected on dust scattering important for significant dust load. The post-Viking H_2O measurements have shown

¹Space Research Institute, Moscow, Russia.

²Service d'Aéronomie, Centre National de la Recherche Scientifique, Verrières-le-Buisson, France.

³Moscow Institute of Physics and Technology, Dolgoprudnyi, Russia.

different results. Earth-based measurements by *Rizk et al.* [1991] have indicated a more humid southern summer than MAWD. On the other hand, the microwave observations by *Clancy et al.* [1992] have shown only one half of the MAWD estimate. These differences have initiated a discussion about an interannual variability of the water cycle on Mars [*Clancy et al.*, 1996].

[5] Thermal Emission Spectrometer (TES) on Mars Global Surveyor (MGS) allows to retrieve the water vapor abundance from the thermal IR spectra using rotational H₂O transitions in the range of 20–40 μm [*Smith*, 2002]. TES systematically monitored several atmospheric parameters during more than two complete Martian years in 1999–2003 [*Smith*, 2004]. The modern climatology of Mars atmospheric water and aerosol is generally based on MGS/TES measurements. MGS/TES data show that the annual climate cycle is generally stable during the reported period. Comparison of thermal infrared data collected by Mariner 9, Viking, and MGS shows a repeatable annual cycle of the midlatitude air temperature, dust opacities and water ice opacities, especially during the north spring and summer [*Liu et al.*, 2003]. Main year-to-year variability with high variations of dust, temperature and H₂O occurs in perihelion season and is related to global dust storms.

[6] Recent ground-based near-IR water vapor measurements by *Sprague et al.* [2006] showed a somewhat lower value compared with TES.

[7] Mars Express, a mission with unique atmospheric capabilities, carries three instruments capable to measure atmospheric water vapor from near-IR to thermal IR spectral ranges. Planetary Fourier Spectrometer (PFS) [*Formisano et al.*, 2005] measures water vapor in both near-IR and thermal-IR spectral ranges at high spectral resolution. Also, from PFS spectra the temperature profile of the atmosphere (crucial for thermal-IR retrievals) and the dust content (needed for near-IR) can be retrieved. Mapping spectrometer OMEGA [*Bibring et al.*, 2004] provides spatially resolved measurements in near-IR, in particular at 2.56 μm with much lower spectral resolution but good S/N. A portion of OMEGA measurements of the water vapor on the north pole is already analyzed by *Encrenaz et al.* [2005a]. The third instrument is SPICAM IR described below. Such a redundancy is worthwhile. Simultaneous use of Mars Express data should allow to continue the monitoring of Mars climate began with MGS/TES, and to validate different techniques of spectroscopic detection of water vapor.

[8] SPICAM IR light-weight spectrometer is primarily dedicated to the measurements of water vapor contents in the Mars atmosphere [*Korablev et al.*, 2006]. The measurement with good spectral resolution (3.5 cm⁻¹) is performed in the near-IR 1.37 μm band, which is mostly free from CO₂ absorption. The band of 1.37 μm was already used in the past. The same band was used by humidity sensor on early Soviet missions to Mars (Mars 3 and 5) [*Moroz and Nadzhip*, 1975, 1976], and by Viking/MAWD experiment [*Jakosky and Farmer*, 1982]. Our data can be therefore directly compared to Viking/MAWD results.

[9] The present paper describes the method and the results of water vapor retrieval from SPICAM IR data. Measurements cover a full Martian year from L_s = 330° (January 2004) to L_s = 340° (December 2005). The accent is

made on retrieval procedure, assumed atmospheric and spectroscopic parameters, and the uncertainties of the result. The seasonal distribution of water vapor is presented and compared to other measurements.

2. Operation Modes of the Instruments and Calibrations Related to H₂O Measurement

[10] The general description, operating modes and observations of SPICAM IR can be found in *Korablev et al.* [2006]. SPICAM is a very light 0.8 kg spectrometer on the principle of acousto-optic filtration (AOTF) of light. It has high enough spectral resolution to resolve features of H₂O absorption in the solar light reflected from the planet in the 1–1.7 μm range. Field of view of the instrument for nadir observations is 1° corresponding to 4.5 km from the pericenter of Mars Express orbit.

[11] On Figure 1 we present the two typical raw spectra recorded by SPICAM IR in two operating modes mostly used for nadir observation. In the first mode a complete spectral range is scanned by AOTF with fine spectral sampling. Integration time for one spectral point equals 5.6 ms, AOTF RF power 1504, and gain factor 8.25. In this mode the registration of a spectrum (3984 spectral points) takes about 24 sec. During this time the line of sight (LOS) of the instrument spans ~150 km on the surface. During an orbit covering 50°–100° of latitude, only 40–70 spectra are recorded. To achieve shorter measurements, we scan only three portions of the spectrum with H₂O and CO₂ bands, O₂ emission, and also the H₂O and CO₂ ice bands (Figure 1, right) (see *Korablev et al.* [2006] for detailed explanation). The positions of the three windows correspond to following spectral ranges: (1) 1440–1465 nm, (2) 1348–1440 nm, and (3) 1258–1285 nm. The number of spectral points equals to 996 and one spectrum is recorded each 6 s. This optimized mode compromising the signal-to-noise ratio and the duration of spectrum record was routinely used for nadir observations starting from orbit 103.

[12] SPICAM IR uses synchronous detection of signal. Background signal is subtracted from useful signal for each measured spectral point. However, some background signal comes as RF electrical interference originated from AOTF and its driver. This signal depends on RF frequency, power, and environment conditions on the spacecraft. We determined the background signal and to subtract it from the measured spectra (Figure 1) [see *Korablev et al.*, 2006].

[13] The spectral response function of the instrument is determined by the AOTF characteristics. Its width and shape is important, because the H₂O band is not completely resolved in our spectra, and the continuum is uncertain. The spectral response function was measured during calibrations before launch using a spectral line source. The spectral resolution of SPICAM IR AOTF spectrometer is roughly constant if expressed in wave numbers and equals to 3.5 cm⁻¹. In the spectral range of the H₂O band the resolving power $\lambda/\Delta\lambda \approx 2000$. Our resolution is lower than that of MAWD (1.2 cm⁻¹), but we measure well-sampled H₂O band whereas MAWD measured only 5 spectral points. The final radiometric calibration of SPICAM was obtained in flight comparing with simultaneous measurements by OMEGA mapping spectrometer [*Bibring et al.*, 2004]. The sensitivity

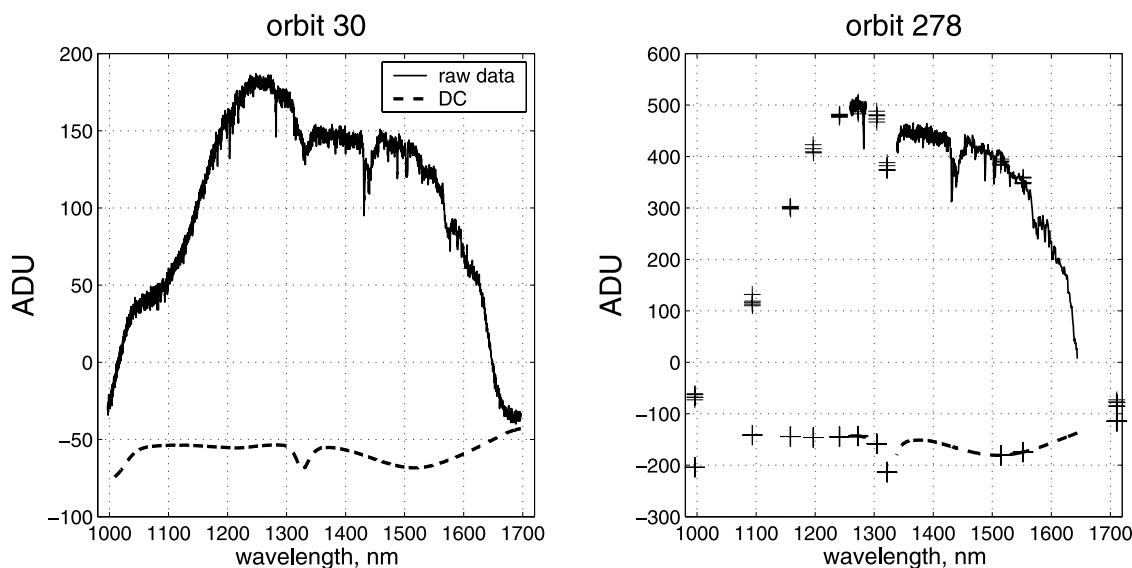


Figure 1. Two main modes for nadir observations. (left) Full spectrum, raw data (solid line) and dark signal (dashed line). Raw data are in ADU (instrument counts), 3984 spectral points, DAC (AOTF RF power) 1504, integration time 5.6 ms, gain 3, duration 24 s. This mode was used for first orbits up to number 103. (right) Three windows and DOT set number 3, 996 spectral points, DAC 1744, integration time 5.6 ms, gain 8.25, duration 6 s. Standard mode is used for all nadir observation after 134 orbit. The three windows are dedicated to specific targets: CO₂ band in 1.43 μm , H₂O 1.37 μm , and O₂ 1.27 μm .

of the spectrometer defined by the noise equivalent brightness (NEB) is $\sim 0.12\text{--}0.15\text{ W/m}^2/\text{sr}/\mu\text{m}$ in the 1.3–1.4 μm range.

[14] The measurements are performed in parallel with two detection channels, corresponding to different polarization of light. The spectral resolution in the first channel is a little better, and the NEB in the second channel is $\sim 0.25\text{--}0.3\text{ W/m}^2/\text{sr}/\mu\text{m}$, almost two times higher than that in the first channel. The dark signal for the second channel has stronger dependence on the temperature and the accuracy of its calibration is lower. The overall quality of the first channel is better, and we used only the data obtained in this channel for the H₂O retrievals. An example of calibrated spectrum with the water vapor band is presented in Figure 8 of *Korablev et al.* [2006].

3. H₂O 1.37 μm Band: Spectroscopic Data and Modeling

[15] The complete H₂O band extends from 1340 to 1480 nm. We present in Figure 2 synthetic models of water vapor absorption in the rotational-vibrational 1.37- μm band, demonstrating the sensitivity of theoretical band depth to variations of water vapor content in atmosphere. As discussed above, the 1.38- μm band is frequently used for H₂O detection on Mars because the CO₂ absorption within the band is negligible. A set of CO₂ synthetic spectra calculated for different pressures is shown in Figure 3. The range of 1350–1430 nm is mostly free from CO₂ absorption except a small absorption at 1365–1380 nm (Figure 3, bottom) that we account for in the retrieval. The synthetic spectra in Figures 2 and 3 are converted to SPICAM IR resolution. The assumptions for the synthetic model and atmospheric parameters are discussed below.

3.1. Spectroscopic Data

[16] We used HITRAN 2000–2001 database [*Rothman et al.*, 2003], containing 2063 H₂O lines in the range of 1.35–1.43 μm . The line widths given in the database are for water vapor broadened by air. To account for CO₂ broadening of lines in the Martian atmosphere we multiplied the air-broadened half-widths from HITRAN2000 database by 1.3 as was done previously by *Pollack et al.* [1993] for Venus atmosphere basing on the work by *Howard et al.* [1956].

[17] Using line-by-line calculation we constructed a pre-calculated look-up table of H₂O and CO₂ cross sections with 13 values of pressures ranging from 10^{-10} to $2 \cdot 10^{-2}$ bar and 16 temperatures from 100K to 340 K. Linear interpolation was used within the tabulated values. To compute high-resolution absorption we use wave number grid with adaptive step. Minimal step of 0.001 cm^{-1} starts from the center of a line and increases toward line wings. We compute Voigt line profile using the *Matveev* [1972] approximation.

3.2. Solar Spectrum

[18] For the retrieval we need a solar spectrum with spectral resolution higher or equal to the resolution of SPICAM IR (3.5 cm^{-1}). There are few measurements of solar spectrum in the near IR. Earth-based observations are limited to atmosphere transparency windows, our range being unavailable because of strong H₂O absorption. The only two near IR solar spectra available until recently are by *Kurucz* [1995] and *Thuillier et al.* [2003]. Theoretical spectrum by *Kurucz* is sampled at 1 cm^{-1} . The spectrum by *Thuillier et al.* [2003] in the range of 0.2–2.4 μm based on measurements from space (SOLSPEC and SOSP instruments) has a resolution similar to SPICAM IR in our spectral range.

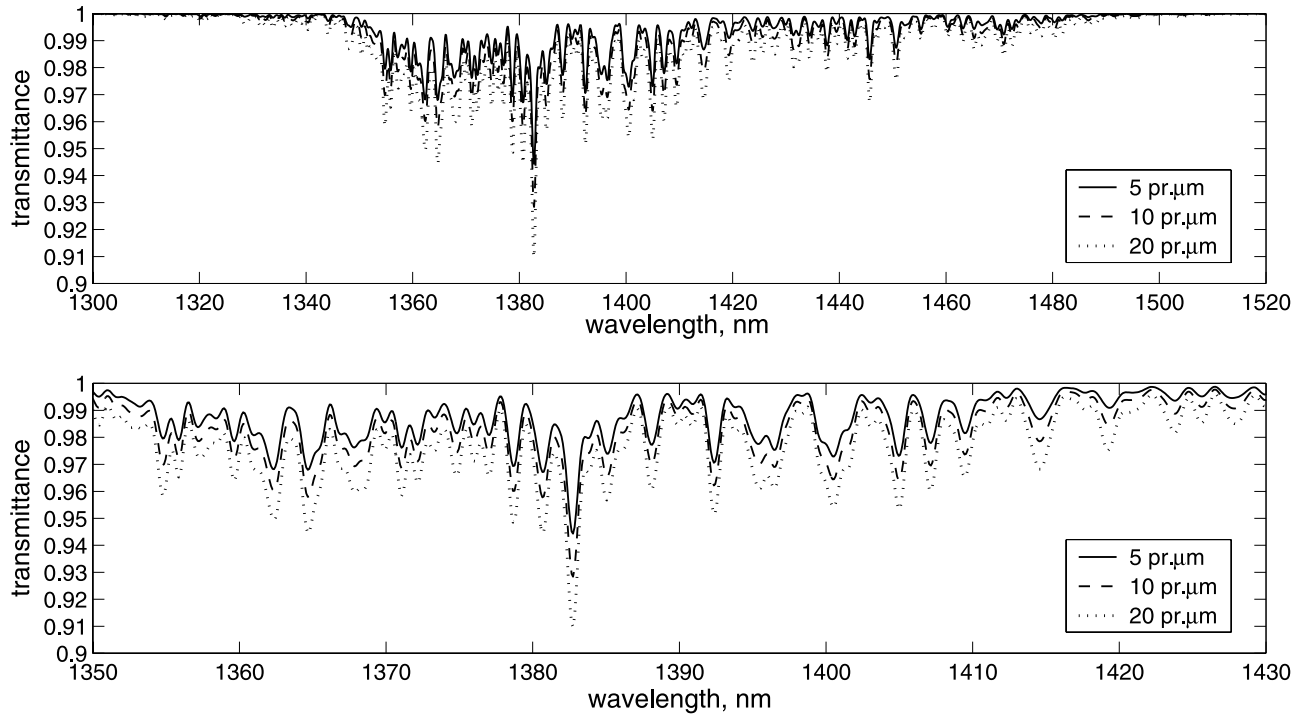


Figure 2. Synthetic models of the 1.38 μm band for different contents of water vapor in Mars atmosphere: 5, 10, and 20 pr. μm . Air mass equals 2. Only the absorption due to H_2O is shown. (top) Full range; (bottom) zoom on the strongest part of the band, corresponding to window 2 in SPICAM spectra.

[19] Recently, *Fiorenza and Formisano* [2005] have published a new spectrum obtained from a combination of ATMOS 2000–4800 cm^{-1} solar occultation data (transmission) and Kitt Peak 4800–8200 cm^{-1} absolute spectra, both measured at very high resolution. We used this solar spectrum for our retrieval.

3.3. Martian Climatology

[20] The information about the surface pressure and temperature profiles in Martian atmosphere was taken from European Martian Climate Database (EMCD) [*Forget et al.*, 1999]. We use 33 altitude levels of pressure and temperature as it is done in the EMCD.

[21] The water vapor profile is assumed to be controlled by saturation level (or hygropause). The saturation vapor pressure is calculated as:

$$P_{\text{sat}} = 6.11 \times \exp \left[22.5 \times \left(1 - \frac{273.14}{T} \right) \right], \quad (1)$$

where P_{sat} is in mbar, and T is the temperature in Kelvin. The formula was taken from *Richardson and Wilson* [2002] and references therein. The altitude of the saturation level is computed using pressure and temperature profiles from the GCM. We assume water vapor uniformly mixed up to the saturation level, and no water vapor ($f_{\text{H}_2\text{O}} = 0$) above this level.

3.4. Radiative Transfer and Basic Assumptions

[22] When computing the synthetic model to compare to a measured spectrum we account only for transmission of the solar light through Martian atmosphere. The intensity of

light at each wave number (monochromatic intensity) is calculated as follows:

$$I_{\lambda} = I_{0\lambda} A \exp(-\tau_{\lambda} \times (1/\mu + 1/\mu_0)), \quad (2)$$

where $I_{0\lambda}$ is the solar intensity, μ and μ_0 are cosines of emission and solar zenith angles, respectively, and the atmospheric optical depth is determined as.

$$\tau_{\lambda}(z) = \int_a^{\infty} \chi_{\lambda}(z') dz', \quad (3)$$

where z is the altitude above the surface. The extinction coefficient χ_{λ} equals:

$$\chi_{\lambda}(z) = \sigma_{\lambda}^a(z) + \sigma_{\lambda}^g(z) + \kappa_{\lambda}^a(z) + \kappa_{\lambda}^g(z), \quad (4)$$

where σ_{λ}^a and σ_{λ}^g – aerosol and Rayleigh scattering coefficients, κ_{λ}^a и κ_{λ}^g – absorption coefficient for aerosol and gas. Rayleigh scattering is negligible, but the scattering by aerosol particles, comparable with wavelength is apparent in the near IR range. However, for low observation angles (when the air mass is below 3) the effect is small [*Fedorova et al.*, 2004]. Air mass M characterizes the optical path in the atmosphere: $M = \frac{1}{\mu} + \frac{1}{\mu_0}$. At present we neglect the effect of aerosol scattering (except for some test calculations, see below). As a result, the extinction coefficient χ_{λ} is determined only by gas absorption.

[23] Solar flux is dominating in our spectral range, and we neglect the thermal radiation of the surface and the atmosphere. To compare a synthetic spectrum to a spectrum

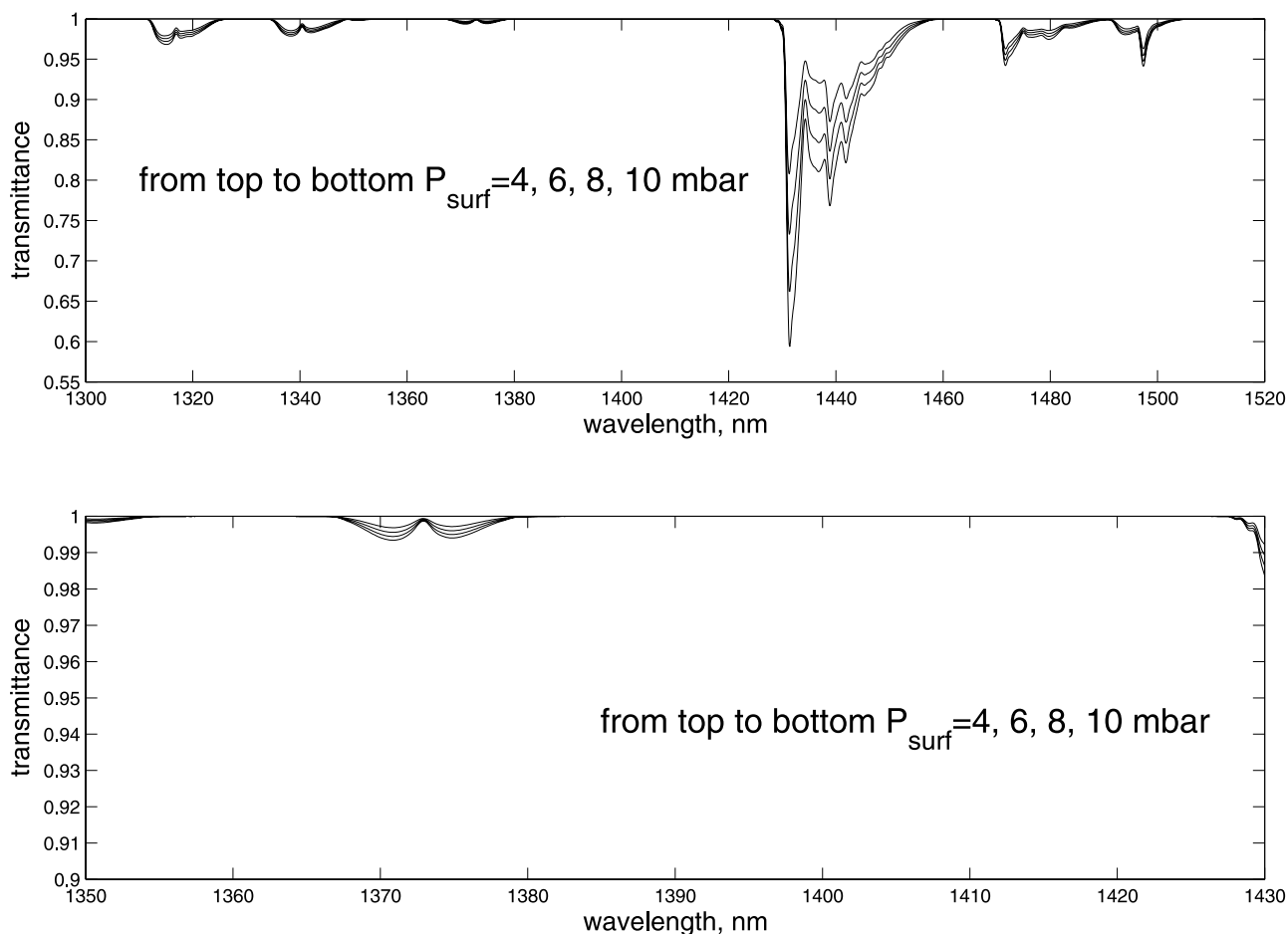


Figure 3. Synthetic model of the CO₂ band for different pressures (from top to bottom: 4, 6, 8, and 10 mbar). The spectral range is the same as in Figure 2. Atmosphere conditions (summer in northern hemisphere) are taken from EMCD [Forget *et al.*, 1999]. Air mass equals 2.

measured by SPICAM we integrate the high-resolution absorption along the optical path in the atmosphere (plane-parallel geometry adequately describing nadir observations is used). Finally we convolve the spectrum according to spectral response function of SPICAM.

4. Retrieval Procedure

[24] For retrieval we employed spectra measured by SPICAM IR in the spectral range 1350–1430 nm consisting of 350 spectral points. This range is almost free from CO₂ absorption (see Figure 3, bottom). We work with calibrated spectra in absolute units (W/m²/μm). To minimize the noise we average 10 adjacent spectra (sliding average), and fit each second spectrum in the following sequence: 1–10, 3–12, 5–14. . .

[25] The H₂O band is not fully resolved in our spectra (Figure 2, bottom), and to determine the equivalent width of the water vapor band we need to define the spectral continuum. The continuum is not flat due to surface albedo and aerosol scattering. In Figure 4, three calibrated H₂O spectra divided by the solar spectrum and normalized to a reflectance value at 1350 nm are presented. Two typical reasons for a distortion of the continuum are shown: a signature of water ice, and a signature of CO₂ ice. Also, some spectral

slope, due to mineralogy features, or merely resulted from the change of the surface albedo during the measurement may affect the continuum, though to a smaller extent than for the given examples. At the same time the H₂O band is very clear on all the three curves, and we need to find a way to estimate spectral dependence of continuum (which is the spectrum of the apparent surface albedo).

[26] The retrieval is complicated by the weakness of the H₂O absorption in the 1.38-μm band. Twofold increase in water vapor abundance (from 10 to 20 pr μm) increases the transmittance for only ~1.5% (for the deepest feature at 1383 nm, see Figure 2). For weaker features within the band the difference is even smaller. Below we present two methods of H₂O retrieval and test its sensitivity to different spectral range inside the band.

[27] In the first method to find the continuum we applied the following procedure.

[28] 1. On the first iteration the continuum is found as $I_{\text{measured}}/(I_{\text{solar}} * \mu_0)$. The resulting reflectance is convolved with a broad function $\cos^2(\pi/2 * (\lambda - \lambda_0)/\Delta\lambda)$. To account for spectral features of ices and do not modulate the atmospheric water band, the half-width $\Delta\lambda$ is chosen = 15 nm.

[29] 2. Using this continuum, initial value of H₂O abundance (20 pr μm) and the solar spectrum from *Fiorenza and Formisano* [2005] we construct a synthetic spectrum in the

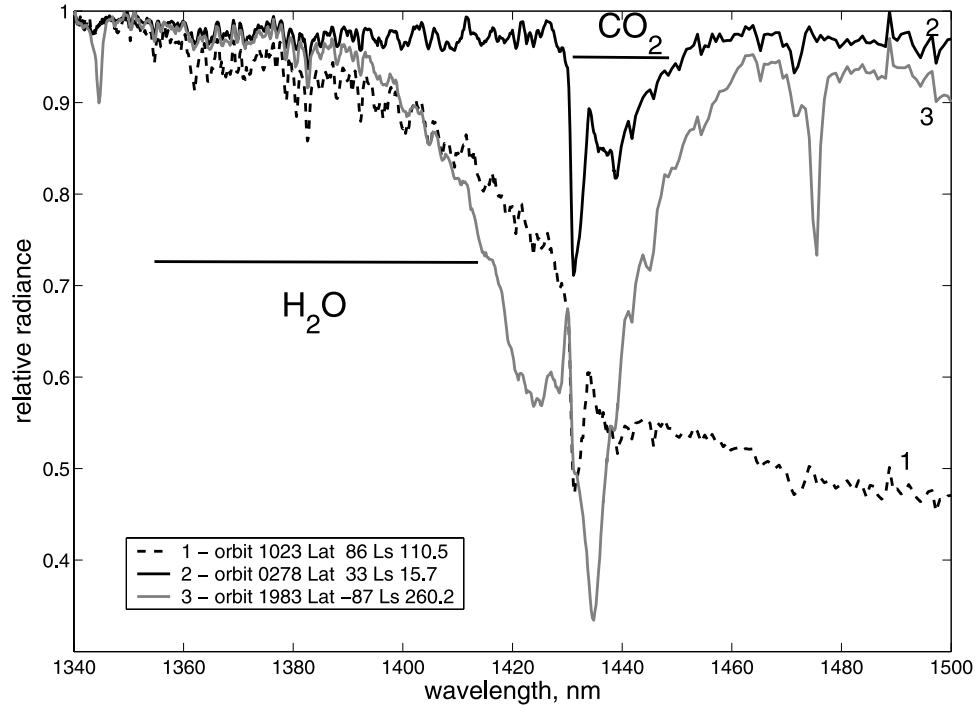


Figure 4. Examples of IR SPICAM spectra recorded for different locations and seasons, demonstrating variations of the spectral continuum within H₂O band. I/R_{sun} are normalized to a value at 1350 nm. Curve 1 corresponds to the north pole. A wide H₂O ice signature from 1340 onward is apparent. Curve 2 corresponds to a low latitude spectrum, possibly slightly distorted by albedo variations. Curve 3 corresponds to the south pole spectrum with signatures of CO₂ ice, modifying the continuum within H₂O band similar to the H₂O ice. The water vapor band at 1.37 μm is apparent in all spectra.

range of 1350–1420 nm to be compared to the measured spectrum. Then we find the best fit continuum spectrum, corresponding to a minimal difference between the model and the observation (2–5 iterations are needed) with fixed H₂O abundance.

[30] 3. We seek for the best fit value of H₂O abundance, constructing a synthetic spectrum with the previously found continuum. Golden section minimization is used. The synthetic spectrum is compared to the measured spectrum, and with an iterative procedure we find again a new best fit continuum spectrum, corresponding to a minimal difference between the model and the observation (2–5 iterations are needed).

[31] 4. The procedure continues in a loop until a convergence with both best fit H₂O value and the continuum spectrum are found.

[32] Let us assume observed intensity: I_i^{obs} as a result of measurement of a real intensity I_i^{real} : $I_i^{\text{obs}} = I_i^{\text{real}} + \varepsilon_i$, where ε_i is a normally distributed random value with mean value of 0 and standard deviation of σ_i . The measurement noise determined by NEB $\approx 0.12 \text{ W/m}^2/\text{sr}/\mu\text{m}$ can be considered as the standard deviation σ . The noise is assumed to be uniform within the range of water vapor band. For average data the uncertainty is $\sigma = \varepsilon/\text{sqrt}(n)$, where n is the number of spectra in the average. We seek for the best fit minimizing χ^2 :

$$\chi^2 = \frac{\sum_{i=1}^N (I_i^{\text{obs}} - I_i^{\text{mod}})^2}{\sigma^2(N-1)}. \quad (5)$$

[33] In the described procedure we could not find the “true” continuum, compromising the spectral variability of such absorbers as CO₂ ice, which has fairly narrow features, and that of water vapor band. Therefore the integral absorption or the equivalent width of the band is not found. Therefore the main information about H₂O absorption at 1.38 μm band consists in relative depth of H₂O spectral features within the band.

[34] We have tested the sensitivity of our results to $\Delta\lambda$. In Figure 5b the comparison of retrieval value for orbit 1000 is presented for $\Delta\lambda = 5, 15, 25 \text{ nm}$. The result is consistent inside 10%. The variation of $\Delta\lambda$ within this range does not affect significantly the results of retrieval.

[35] The uncertainty of H₂O spectroscopy and solar lines (see section 7) could be source of errors during the retrieval in the different spectral range. For comparison we chose four ranges: (1) 1355–1412 nm, (2) 1365–1405 nm, (3) 1365–1395 nm, and (4) 1377–1389 nm. The latter range includes only the deepest H₂O features around 1380 nm. The comparison is presented in Figure 5a. The results are consistent inside 20–25%, while a systematical difference between wider and shorter ranges is present. The highest H₂O values are retrieved using the shortest range. The fit quality remains good in all cases: examples of the fitting for same spectrum but for three ranges are shown in Figure 6.

[36] The second retrieval method consists of using a relative depth of main H₂O spectral features in the range of 1360–1410 nm. The relative depth is defined as $r_i = I_{i_{\text{center}}}/(I_{i_{\text{cont1}}} + I_{i_{\text{cont2}}})$. We find the same relative depth

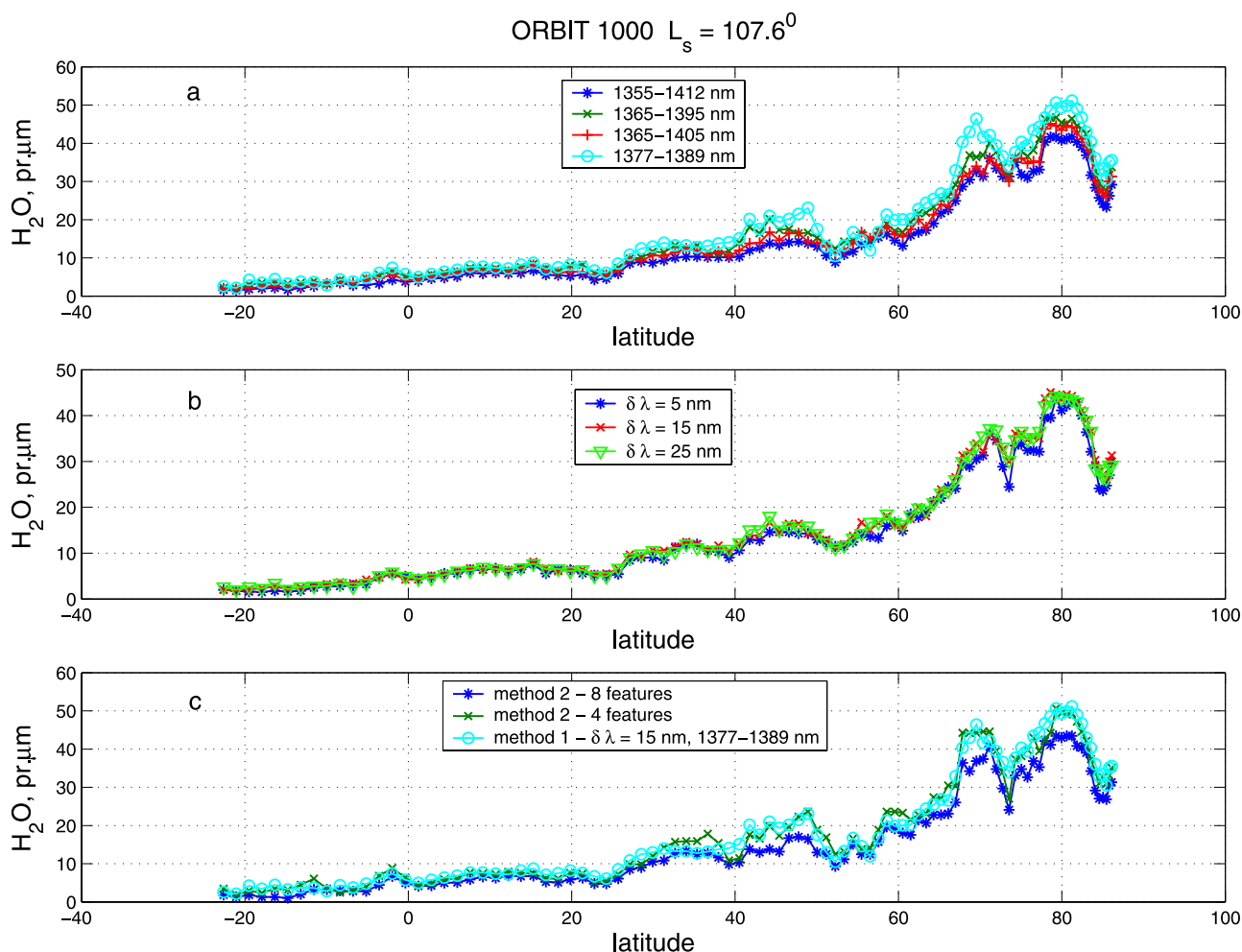


Figure 5. The comparison of retrieval results on orbit 1000 ($L_s = 107.6^\circ$) for different fitting methods (see text). (a) Different spectral ranges for method 1. (b) Different $\Delta\lambda$ continuum parameter (method 1): 5, 15, and 25 nm. Spectral range is 1365–1405 nm. (c) Method 2 with different number of relative depths of H_2O features. Green curve is four sharp features in the range of 1377–1389 nm that almost coincide with cyan curve (narrow range 1377–1389 nm around sharp features with method 1).

r_i^{mod} in a model spectrum and minimize the difference of $\sum_{i=1}^N (r_i^{\text{obs}} - r_i^{\text{mod}})^2$ to retrieve the H_2O value using golden section method. To test the sensitivity on different features we used two variants of this method: 4 sharp features in the range of 1377–1389 nm (1378.5, 1381, 1383 and 1388 nm), and 8 sharp features in the range of 1360–1410 nm (1365, 1378.5, 1381, 1383, 1388, 1393, 1400 and 1405 nm). On the average, the first combination results in 20% more H_2O abundance compared to the second one.

[37] As in the first method, a more narrow spectral interval centered on the strongest H_2O features results in larger retrieved H_2O abundance. It is conceivable that retrieval in a wider spectral range, although improves the accuracy statistically, tends to systematically underestimate the H_2O abundance. The integral absorption of H_2O might be compensated due to continuum adjustment, while the sensitivity to the differential absorption is weaker on the edges of the band. Weaker features are subject to stronger systematic errors due to, e.g., imperfect solar spectrum or H_2O spectroscopy.

[38] The results of retrieval with the two different methods coincide within 5–10% for the same spectral ranges (Figure 5c). The difference among the two methods is small because both are based on the relative depths of absorption features. Because of much larger number of spectral points involved into fitting the first method is statistically more accurate. The statistical uncertainty of the retrieved water vapor varies from 5 to 40% depending on signal-to-noise ratio in average spectra. The sensitivity of the results to different factors is discussed in section 7.4.

[39] Below we present results retrieved for the spectral range of 1365–1395 nm and $\Delta\lambda = 15$ nm.

5. Results

[40] The total column abundance of H_2O in precipitable microns is routinely produced for each Mars Express orbit when SPICAM IR was operational. The results could be sorted according to geographic location, local time and season. The observations presented here are limited to first Martian year of Mars Express from 2004 January ($L_s = 330^\circ$)

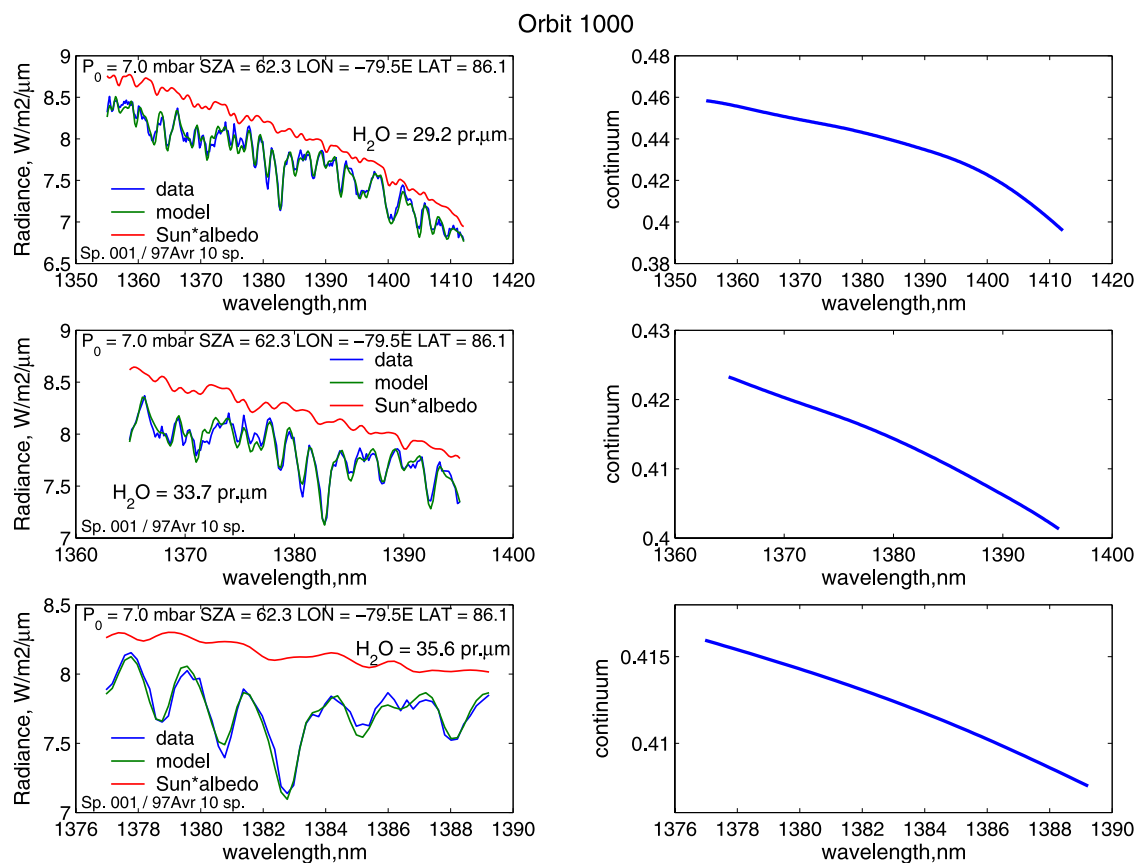


Figure 6. Examples of fits to the SPICAM IR data in the H_2O absorption band at $1.38 \mu\text{m}$. The same average spectrum for nadir orbit 1000 is fitted for different spectral ranges (from top to bottom): 1355–1412 nm, 1365–1395 nm, and 1377–1389 nm. Blue curve, SPICAM IR calibrated data; green curve, synthetic fit; red curve, Sun spectrum modified because of surface albedo (a wide H_2O ice band causes an additional absorption longward from 1420 nm). The retrieval continuum is also shown.

to 2005 December ($L_S = 340^\circ$). During this period 752 successful nadir orbits were made. Some seasons are missing and shown as blanks at seasonal map. At $L_S = 75^\circ\text{--}90^\circ$ the pericenter was on the night side, at $L_S = 200^\circ\text{--}240^\circ$ the observations were interrupted because of radar antenna deployment.

5.1. Seasonal Map by SPICAM

[41] A seasonal distribution of water vapor column density observed by SPICAM IR is presented in Figure 7 in function of latitude and season. Results are zonally averaged into bins of 2° in latitude and 2° in L_S . Figure 7 (top) corresponds to a full data set retrieved from SPICAM measurement. Figure 7 (bottom) presents observation where dust influence is minimal: we only show the results when the observation and solar zenith angles are below 60° (see section 7).

[42] The maximal value of water vapor is observed at north pole at $L_S = 110^\circ\text{--}120^\circ$ (north pole maximum, NPM) is $55 \text{ pr } \mu\text{m}$. At $L_S = 120^\circ$, water vapor abundance monotonically decreases from north to south, from $25\text{--}35 \text{ pr } \mu\text{m}$ at 60°N to $12\text{--}15 \text{ pr } \mu\text{m}$ at 40°N and $<6 \text{ pr } \mu\text{m}$ at equator. After $L_S = 130^\circ$ water vapor declines rapidly at high northern latitudes, falling below $12 \text{ pr } \mu\text{m}$ at $L_S = 150^\circ$. We do not have high-latitude north observations later in this

season. The maximum of water vapor shifts to low latitudes and reaches $30^\circ\text{--}35^\circ\text{N}$ at $L_S = 150^\circ$ with the abundance of $12\text{--}14 \text{ pr } \mu\text{m}$. The broad equatorial maximum of H_2O extends trough $L_S = 175^\circ\text{--}205^\circ$ with the abundance as high as $9\text{--}13 \text{ pr } \mu\text{m}$. There is not enough data to trace the maximum in H_2O at $L_S = 0^\circ\text{--}30^\circ$ persisting throughout the northern fall and winter until $L_S = 40^\circ$ as a function of latitude. We see a part of this maximum at $L_S = 270^\circ\text{--}340^\circ$ with the water vapor value of $7\text{--}9 \text{ pr } \mu\text{m}$. This maximum is clearly distinguishable in Figure 7 (bottom). On Figure 7 (top) a part of this maximum could be masked by dust due to high observation angles.

[43] In the southern hemisphere we observe a gradual rise in H_2O . The maximum of H_2O abundance is reached at $L_S = 270^\circ\text{--}310^\circ$ and $70^\circ\text{--}80^\circ\text{S}$ of latitude and corresponds to $13\text{--}16 \text{ pr } \mu\text{m}$.

[44] The latitudinal dependence of water vapor shows a local minimum at $10^\circ\text{--}30^\circ\text{S}$ ($4\text{--}6 \text{ pr } \mu\text{m}$) and the already mentioned local maximum at $0^\circ\text{--}30^\circ\text{N}$. This feature can be explained by the H_2O transport from the south hemisphere to the north hemisphere due to Hadley circulation.

5.2. Geographical Distribution of Water Vapor

[45] In the beginning of the mission observations were scarce, and whereas the seasonal coverage was adequate, the spatial coverage was poor. However, starting from $L_S =$

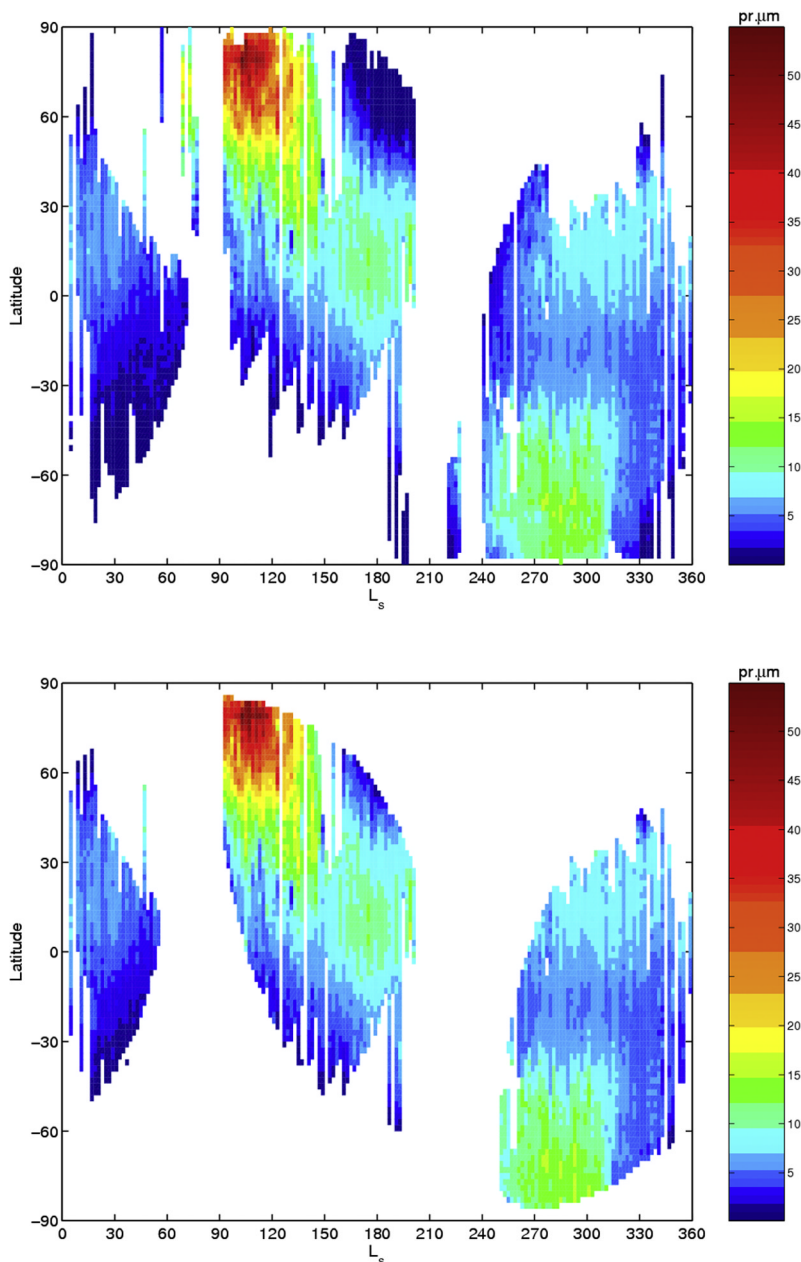


Figure 7. A seasonal map of H_2O distribution by SPICAM. (top) Full set of SPICAM measurements for the first Martian year; (bottom) data subset limited to emission and solar zenith angles $<60^\circ$.

90° the nadir observations were made more often and the coverage became much better. We can compare our results with water vapor maps obtained by TES, though the mapping orbit of MGS is much more favorable for such measurements. *Smith* [2004] presented the interannual comparison of geographical water vapor during two Martian years for $L_S = 285^\circ\text{--}305^\circ$ (MY 24, 25) and three year for $L_S = 105^\circ\text{--}125^\circ$ (MY 24, 25, 26). We present our geographical distribution in same style to reveal eventual differences and similarities with our year of observation (MY 27). Results have been averaged into bins of 2 degrees in longitude and 2 degrees in latitude. Figure 8 presents SPICAM water vapor maps styled following *Smith* [2004, Figure 17]. Water vapor column abundance (in precipitable microns) was scaled

to an equivalent 6.1 mbar pressure surface. Figure 8 (top) corresponds to the scaled water vapor abundance from $L_S = 104^\circ$ to 123° , bottom one at $L_S = 285\text{--}305^\circ$.

[46] The most noticeable feature is that SPICAM reveals absolute values 1.5–2 times lower than TES.

[47] At $L_S = 104^\circ\text{--}123^\circ$ our distribution is the similar to that of TES, while the coverage is significantly worse. Close to the north pole ($80^\circ\text{--}90^\circ\text{N}$) SPICAM water is 1.5 smaller than at $60^\circ\text{--}80^\circ\text{N}$. This feature is not present in TES data for three years and might be explained by aerosol effect at large observation angles (section 7). During the southern summer we observe a H_2O behavior similar to MY 24. A maximum is clearly seen near the longitudes of $90^\circ\text{--}180^\circ\text{E}$ and $90^\circ\text{--}180^\circ\text{W}$, a local maximum at 90°W and

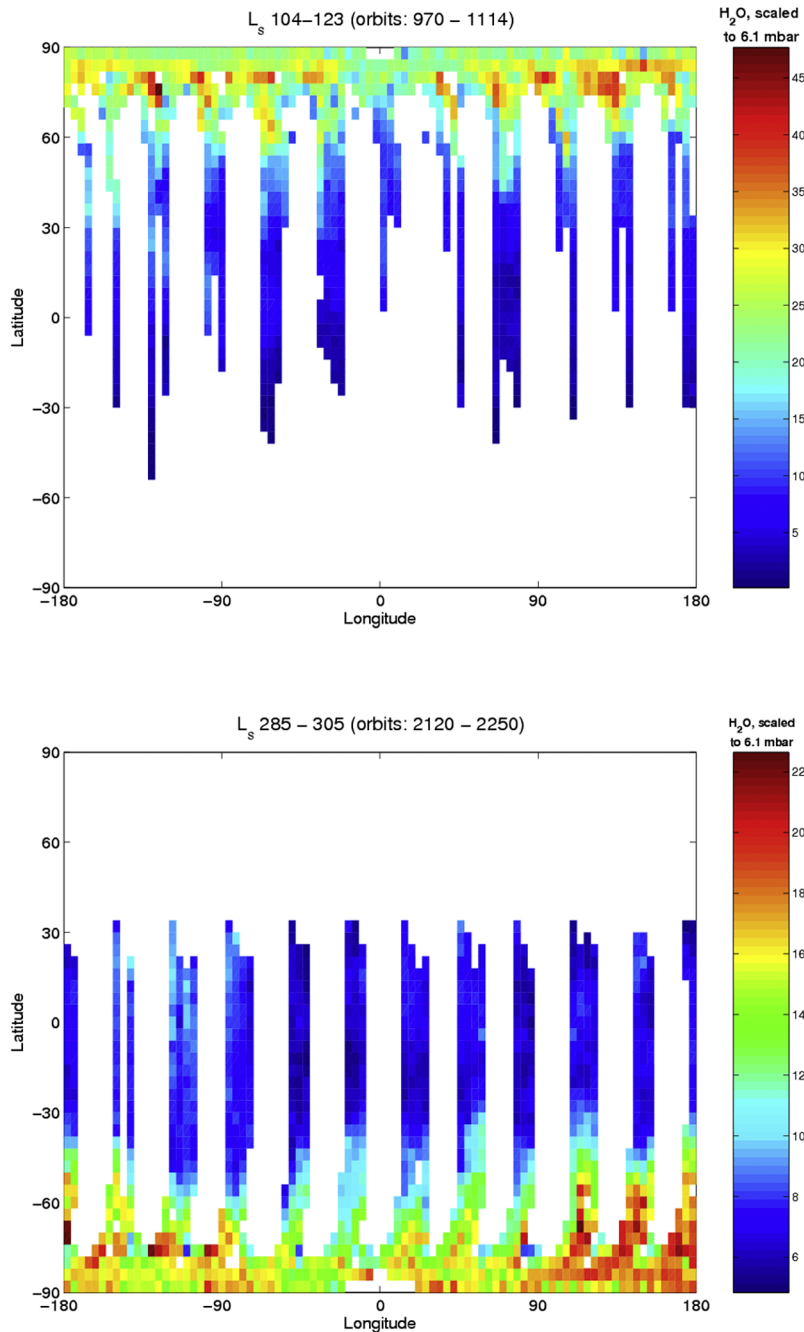


Figure 8. Latitude/east longitude maps of water vapor column abundance (in precipitable microns) scaled to an equivalent 6.1 mbar surface pressure to remove the effect of topography. Two seasons are presented. (top) $L_s = 104^\circ\text{--}123^\circ$ (October–November 2004). (bottom) $L_s = 285^\circ\text{--}305^\circ$ (September–October 2005). All data correspond to MY 27.

$20^\circ\text{--}30^\circ\text{N}$ is barely visible and do not exceed $10\text{ pr } \mu\text{m}$. The MY 24 corresponds to a low dust loading, which is apparently the case in MY 27 [Smith *et al.*, 2006].

6. Comparison of the Seasonal Distribution With Other Data Sets

[48] Our result on the seasonal distribution of water vapor abundance can be compared to observations of Viking [Jakosky and Farmer, 1982] and TES [Smith, 2002, 2004],

ground-based data [Sprague *et al.*, 2006], and recently published analysis of OMEGA data [Encrenaz *et al.*, 2005a]. TES and MAWD H₂O abundances were obtained for a full year and interannual variability could be seen from comparison with these data sets. Comparison with MAWD is of special interest because the same near-IR absorption band is used for the retrieval and the atmospheric effect should be the same. Ground-based observations are limited in seasonal coverage, but different spectral ranges and retrieval techniques of ground-based observations give additional informa-

tion for comparison. OMEGA data obtained on the same spacecraft in the near-IR 2.56- μm band can be used for direct comparison because the measurements coincide in time and location.

6.1. Northern Hemisphere Summer

[49] Both MAWD and TES observations have shown a strong north pole maximum around 80–100 pr μm at $L_s = 100^\circ$ – 120° [Smith, 2004, Jakosky and Farmer, 1982]. The north maximum does not exactly repeat during Viking observation and two years of MGS although the difference is less pronounced at this season than in the southern summer. The water vapor abundance during this maximum exceeds our average value of 54 pr μm up to 1.7 times. In the same time OMEGA measurements of the north pole [Encrenaz et al., 2005a] indicate the maximum of about 55 pr μm , which is consistent with our results. Encrenaz et al. indicate an uncertainty of 30% in the 2.56- μm measurements at the north pole depending upon the continuum level. Ground-based observation [Sprague et al., 2006] supports high water vapor abundance up to 75 pr μm on the average.

[50] Typical midlatitude (40°N) values are 20–25 pr μm as measured by OMEGA and MAWD, and a little higher value of about 25–30 pr μm as measured by TES. These values are by a factor of 1.6–1.8 higher than ours. At 60°N TES values range from 40 to 50 pr μm for $L_s = 90^\circ$ – 115° . MAWD indicates a little lower value of 35–45 pr μm for same season, and H_2O content derived from OMEGA is 25–45 pr μm consistent with MAWD, and a little lower than TES. Our results are ~ 1.5 times lower, varying from 20 to 35 pr μm . Near the equator our values are again lower and correspond to 5–6 pr μm , compared to 10 pr μm by MAWD and 12 pr μm by TES. During the north tropical maximum we also observe lower H_2O abundance compared to other data sets. Our maximal value corresponds to 10–13 pr μm that is 1.8 times lower than 20–22 pr μm from TES and 1.6 times lower than 16–18 pr μm from Viking. The MAWD measurements for $L_s = 206^\circ$ were confirmed from the Earth by TEXES observations: 17 ± 9 pr μm [Encrenaz et al., 2005b]. At $L_s = 150^\circ$ – 160° , both the Pathfinder [Titov et al., 1999] and the SWAS experiment [Gurwell et al., 2000] found low water vapor abundance of 6–8 pr μm . These results are more consistent with the value of 10–12 pr μm measured by SPICAM at 0° – 20°N for this season. A new set of Earth-based observations shows 20% lower value than TES exactly for same time of observation (June 1999) at $L_s = 147^\circ$ [Sprague et al., 2006]. However, this result is still by a factor of 1.5 higher than SPICAM.

[51] We can conclude that water vapor distribution measured by SPICAM is qualitatively consistent with MAWD and TES (and OMEGA at low latitudes), but the absolute values are by a factor of 1.5–1.8 lower. On the other hand the Mars Express measurements of the north pole maximum by OMEGA and SPICAM coincide that do not support a straightforward assumption about a systematic underestimation of water in SPICAM data.

6.2. Southern Hemisphere Summer

[52] The most variable feature of the water cycle on Mars is the south polar maximum occurring in summer in the southern hemisphere. TES observations indicate a maxi-

um of 30–40 pr μm near the south pole (80° – 90°S) at $L_s = 280^\circ$ – 310° . Year-to-year changes in water vapor from TES have larger amplitude than for northern maximum. Water vapor abundance was 20–30% higher during MY24 at 60° – 70°S than during MY 25 with a maximal value of 25–30 pr μm . MAWD has shown a very low value of water vapor abundance with maximum of 10–15 pr μm at 40° – 60°S latitudes and $L_s = 250^\circ$ – 270° . This lower value was linked to the two dust storms observed during the Viking mission near the perihelion (areocentric solar longitude $L_s \sim 205^\circ$ and $\sim 275^\circ$) [Martin and Richardson, 1993]. Using a dust distribution from Viking the new H_2O retrieval from MAWD data was made taking into account a multiple scattering by dust [Fedorova et al., 2004]. The southern maximum of H_2O have increased up to 20 pr μm at $L_s = 270^\circ$ – 280° , still remaining two times lower than TES result. The value obtained by SPICAM is 13–16 pr μm at $L_s = 280^\circ$ – 310° . The location of the maximum coincides with TES but the absolute value is lower by a factor of 2. The difference with the location of the maximum measured by MAWD could be explained by low dust loading for MY27 as compared to a time of Viking observation. Ground-based observations generally confirm the value of southern H_2O maximum of 20–30 pr μm [Sprague et al., 2006; Barker et al., 1970].

[53] Mariner 9 IRIS measurements reported the abundance of 10–20 pr μm at $L_s = 297^\circ$ – 321° at the south pole [Hanel et al., 1972]. Ignatiev et al. [2002] have revisited of this observation after correction for an instrumental effect. Maximum value of 10 pr μm was obtained at $L_s = 290^\circ$ – 310° for 50° – 70°S , which is a little smaller than our 13–16 pr μm . From $L_s = 310^\circ$ to 345° the H_2O abundance decreases to 3–5 pr μm that is consistent with our results.

7. Discussion

[54] The uncertainty on our results may originate from several sources: spectroscopic data set and CO_2 broadening coefficient, solar spectrum, atmospheric data set, surface pressure and water saturation level, radiative transfer in dusty and cloudy atmosphere, and instrumental calibration uncertainties. The transmittance of the 1383 nm H_2O absorption feature changes only for 1.3% when the abundance changes from 5 to 10 pr μm and for 1.5% when the abundance changes from 10 to 20 pr μm (Figure 2). The signal-to-noise of SPICAM is rather high (20–150) that allows a good accuracy to measure H_2O . However, systematic uncertainties due to assumptions listed above are much higher.

7.1. Spectroscopic Database and Solar Spectrum

[55] Spectroscopic data set could be potential source of systematic error. Many papers were dedicated to studies of 1.38 μm H_2O transitions [Parvite et al., 2002; Durry et al., 2005]. Still, the line strengths in HITRAN have large uncertainties, so that the discrepancy between laboratory measurements of line strengths and HITRAN 2000 data reaches 40% for some lines. A new release of HITRAN was published in 2004 [Rothman et al., 2005]. It contains 3499 H_2O lines in the range 1.35–1.43 μm (compared to 2063 lines in previous release), with the strengths and half-widths of lines being more consistent with new measurements. A comparison of transmittance within H_2O 1.38 μm

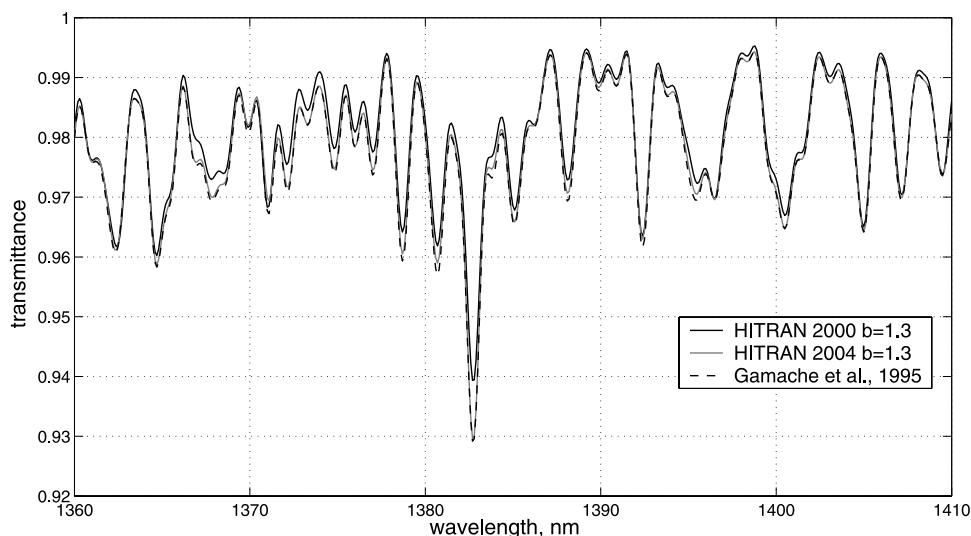


Figure 9. A comparison of synthetic model of the 1.37- μm water vapor band for different absorption coefficients calculated with HITRAN 2000, HITRAN 2004, and *Gamache et al.*'s [1995] line broadening in CO_2 . Line strengths for *Gamache et al.* [1995] are from HITRAN 2004. Air mass equals 2. Surface pressure is 5.2 mbar. Water vapor is uniformly mixed in atmosphere.

band calculated for same condition but for different data sets is presented in Figure 9. The features in spectrum calculated with HITRAN2004 are deeper than with HITRAN2000. The transmittance of features increases from 0 to 0.8%. As a result, the amount of water vapor retrieved with HITRAN2004 is systematically by 20–25% smaller than with HITRAN2000. Figure 10 (top) demonstrates the comparison of retrievals with different spectral database versions.

[56] The widths of spectral lines broadened by CO_2 are not known well. Laboratory measurements of CO_2 broadening in the near-infrared were made by *Gamache et al.* [1995]. The authors compare their laboratory measurements of CO_2 -broadened half-widths with some recent experimental work and theoretical calculations, and investigate the resulting temperature dependence of the half-widths. A scaling coefficient from air-broadening varies from 1.3 to 2.0, depending on a particular transition. Some individual water vapor lines observed at 1.37 μm band are highly saturated in the Martian atmosphere, and higher broadening ratio results in lower retrieved water abundance, than what would be obtained with 1.3 ratio. However, the saturation in the 1.37- μm band is much smaller comparing to stronger H_2O bands such as 2.56 μm and 20–40 μm , and the effect of broadening in our data is limited to a few percents, unless a large amount of water vapor is concentrated in the low atmosphere, as during the north pole maximum. A comparison of water band calculated with HITRAN 2004 line widths multiplied by 1.3 and with *Gamache et al.*'s [1995] line widths is presented in Figure 9. The effect is minor comparing with the difference due to spectroscopic database.

[57] In this paper we present calculation with HITRAN2000 database, used for the data interpretation from the beginning of the mission. In the future we plan to reprocess the entire data set using new HITRAN2004 database, and broadening coefficients from *Gamache et al.* [1995]. The expected effect is systematic (yet smaller water vapor

amount) and would have a little influence on the spatial and seasonal distribution of water vapor.

[58] Solar spectrum could also be a source of systematic error. The depths of solar features in the model spectrum vary from 0.5 to 1%. The uncertainties of solar spectrum can cause the error of up to 2–3 $\text{pr } \mu\text{m}$ that is significant for small H_2O abundance (<5 $\text{pr } \mu\text{m}$).

7.2. Vertical Distribution of Water Vapor and Atmospheric Data Set

[59] The vertical distribution of water vapor is a potential source of errors in retrieved H_2O abundance. In Figure 10 (bottom) we present a comparison of retrieval results at $L_s = 106$ (orbit 987) for two different vertical distributions of H_2O . One of the curves corresponds to a water vapor well mixed in atmosphere from the surface to 100 km. Another curve corresponds to H_2O , well mixed from the surface to altitude where water vapor saturates (see section 3.3). The difference is as high as 20–30% at the north pole and 5–10% for low latitudes. Indeed, different saturation levels affect the number of molecules at low altitudes where the pressure is large. As a result, line widths and therefore the depths of the band for same amount of water are different. For south pole this effect is not so significant because of high saturation level of about 40 km, smaller amount of water and lower pressures.

[60] If the water vapor is not uniformly distributed below the saturation level and a large amount of water is located near surface, retrieved H_2O column density could be decreased. On the other hand, if the water vapor mixing ratio increases with the altitude, the retrieved value of H_2O is higher for the same band depth. To the moment the experimental information about water vapor distribution is not sufficiently detailed. The analysis of the vertical distribution of water vapor by *Rodin et al.* [1997] is consistent with an assumption that water vapor profile is uniform up to the

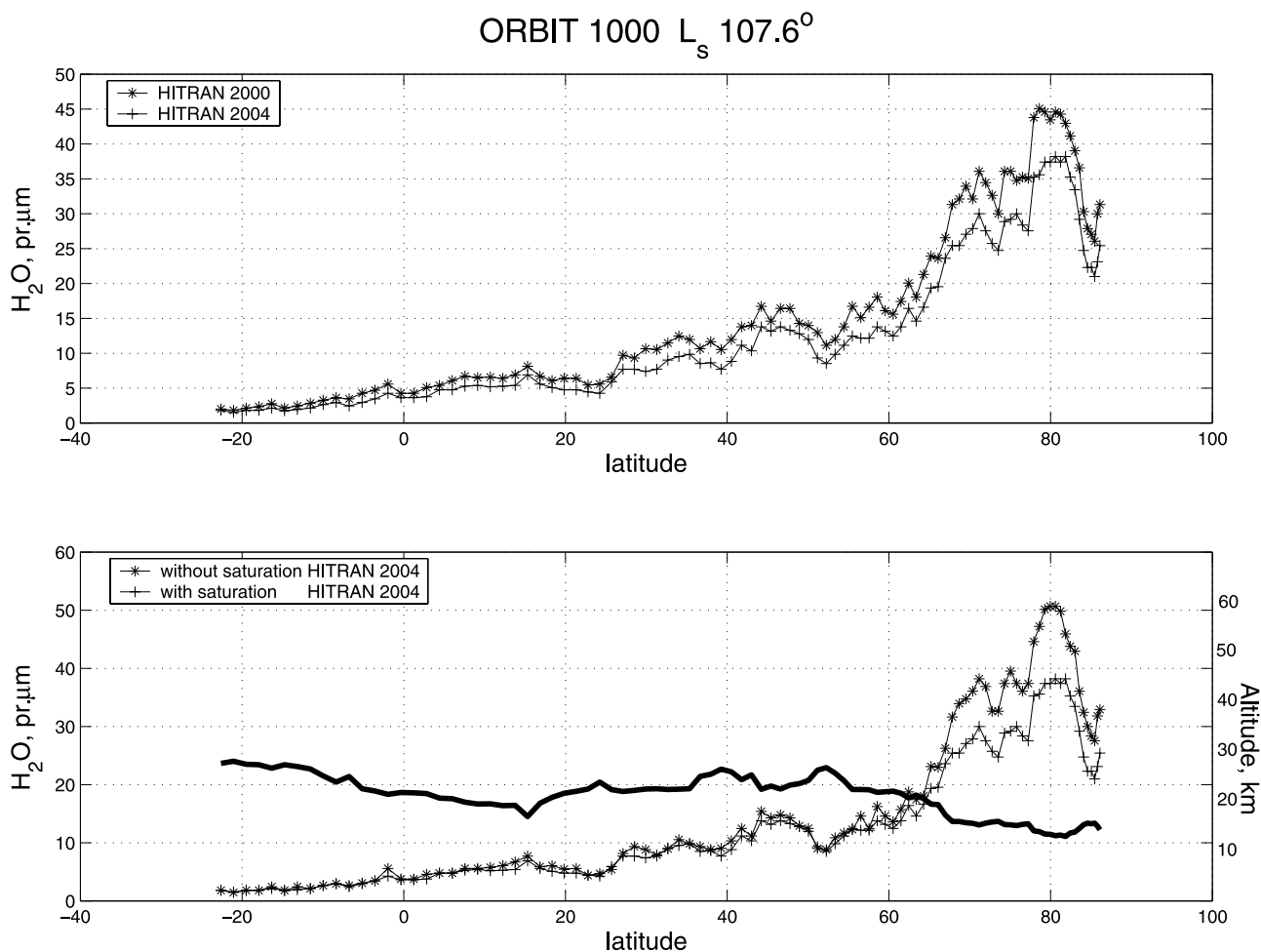


Figure 10. A comparison of H_2O retrieval for orbit 1000 ($L_s = 107.6^\circ$, northern hemisphere summer). (top) For different databases: HITRAN 2000 and 2004. (bottom) For different vertical distribution of water vapor; see text. Thick curve indicates the saturation level.

saturation level. GCMs [Richardson and Wilson, 2002, Montmessin *et al.*, 2004] predict more diverse behavior of water vapor, including strong confinement to the surface near the north pole in aphelion and some inversion in the equatorial regions during the solstitial seasons. However, the difference between model profiles and simplest one adopted in this work does not exceed a factor of 2. Therefore the error in water column retrievals associated with uncertainty in vertical profile may not be significant.

[61] The altitude of H_2O saturation is determined by temperature profile. A reasonable improvement to our retrieval procedure would be the use of temperature profiles retrieved from PFS thermal IR spectra measured simultaneously with SPICAM data instead of the EMCD profiles. Such simultaneous measurements are available in most cases, and we plan to implement the PFS temperature profiles in the future. Of course, the example illustrated in Figure 10 presents an extreme case (uniformly mixed water vapor), and a real difference due to an uncertain temperature profile would be much smaller.

[62] Assuming a warmer temperature profile results in higher values of retrieved water abundance. The effect of thermal profile in SPICAM retrievals is opposite to the situation met by Clancy *et al.* [1996], who had to suppose

colder atmosphere conditions to fit microwave observations of individual rotational line and obtained higher water vapor abundance with colder temperature profile.

[63] Atmospheric pressure might have also some influence on the retrieval. We used surface pressure directly from EMCD [Forget *et al.*, 1999]. The spectral range of SPICAM IR includes relatively weak CO_2 band at 1.43–1.45 μm (Figure 3), which could be used for measurement of surface pressure providing a “true” reference for calculation of water vapor at 1.37 μm . We have calculated surface pressures from 1.43- μm CO_2 absorption for some orbits, and the results are systematically 0.8–1.0 mbar lower than EMCD predictions. We will present a possible explanation in section 7.4.

7.3. Scattering by Aerosol

[64] The influence of atmospheric aerosol on the retrieval of gaseous components in the Martian atmosphere from near-IR bands is known from Viking times [Davies and Wainio, 1981; Jakosky *et al.*, 1988; Hunten *et al.*, 2000; Sprague *et al.*, 2001]. The scattering by dust and cloud particles can screen the lower part of the atmosphere and decreases the apparent near IR absorption by water vapor. This effect is especially important during the dusty season near the perihelion. To accurately account for dust we need

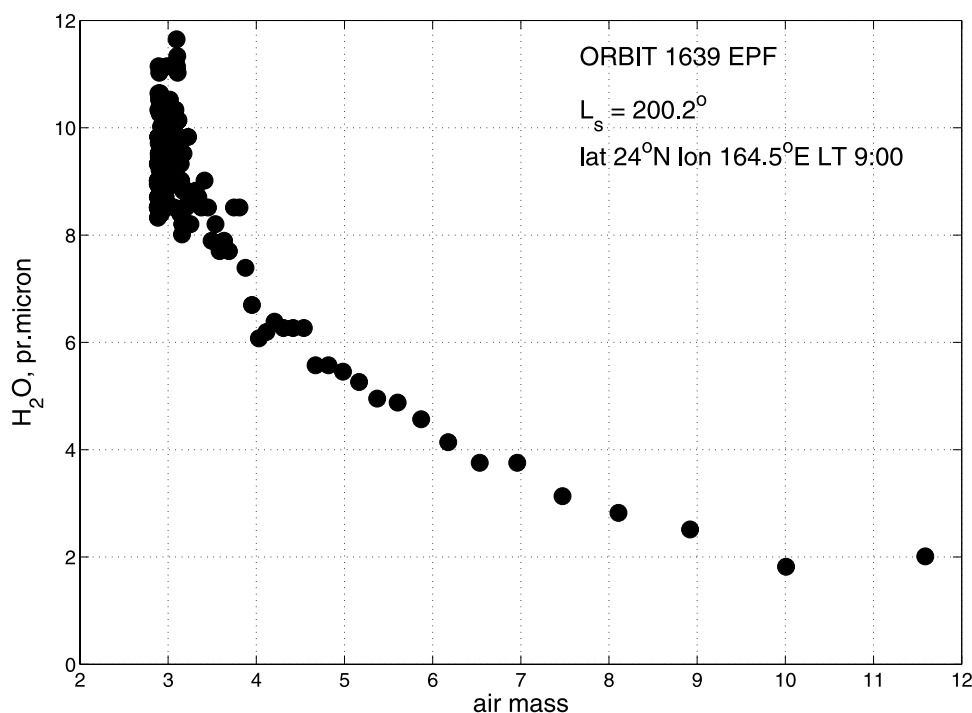


Figure 11. Water vapor abundance retrieved from spot pointing observation on orbit 1639 ($L_s = 200.2^\circ$) as a function of air mass. A much lower abundance is retrieved for large air masses.

an estimation of the aerosol optical depth for all SPICAM observations. TES measurements are available for only a part of SPICAM observations (until 31 August 2004). No data about seasonal distribution of dust and clouds for MY 27 is published so far. PFS on Mars Express is capable to measure dust (in the 9- μm band) and water ice clouds (in the 12- μm band) Some results for three orbits in the beginning of mission (orbits 37, 41, and 68) are published [Zasova *et al.*, 2005]. The opacities reported for these orbits are 0.25 ± 0.05 , corresponding to a visual opacity of 0.5–0.7 [see, e.g., Clancy *et al.*, 2003], and should not have a significant effect on our retrievals [Fedorova *et al.*, 2004].

[65] There is a possibility to estimate the optical depth of dust using 1.43- μm CO_2 band in SPICAM data (Figure 3). The integral absorption of the band is influenced by a number of parameters, such as atmospheric pressure, optical path in the atmosphere and dust opacity. Increasing the pressure and the air mass results in increasing of the band depth, whereas dust by itself could mask CO_2 molecules and decreases the band depth for a large air mass. To estimate the dust optical depth using CO_2 band we need to know the surface pressure with an accuracy of 0.2 mbar. Also, even a small amount of stray light in the spectrometer, unless well quantified, prevents from deducing the dust amount from CO_2 absorption.

[66] The best way to estimate the influence of dust on the near-IR spectrum is spot pointing or emission phase function observations. Mars Express has performed a series of such observations with all remote sensing instruments. These observations should be a theme of a separate research due to a huge amount of information about the surface and dust properties. We consider one such observation with SPICAM IR. On orbit 1639 the air mass varied from 3 to 12. The geometry of observation is following: $L_s = 200.2^\circ$,

latitude 24° , longitude 164.5° , local time $\sim 9:00$. The choice is also good because $L_s = 200^\circ$ corresponds to the beginning of dusty season on Mars [Smith *et al.*, 2004]. The retrieval of water vapor from this band (Figure 11) indicates a strong decrease of derived H_2O abundance with increasing air mass, illustrating the masking effect of dust. The retrieved H_2O values are very close for air mass below 3.5 and can correspond to real values of water vapor abundance on Mars.

[67] To find the optical depth for this orbit using the 1.43–1.45 μm CO_2 we calculated the equivalent width of this band for different amounts of dust in the atmosphere. The equivalent width of CO_2 band is defined as:

$$W[nm] = \int_{\lambda_1}^{\lambda_2} \left(1 - \frac{I_\lambda}{I_0}\right) d\lambda \quad (6)$$

where I_λ is the light intensity within the band, I_0 is the light intensity in the continuum. We chose a simple model of Martian atmospheric dust. The optical parameters of dust were taken from Ockert-Bell *et al.* [1997]. We assumed the Henyey-Greenstein phase function with the asymmetry parameter $g = 0.63$ and single-scattering albedo $\omega_0 = 0.9$. The dust was exponentially distributed with scale height 10 km. To calculate radiative transfer in scattering atmosphere, we used spherical harmonics discrete ordinate method (SHDOM [Evans, 1998]). Figure 12 demonstrates the dependence of the equivalent width on the air mass for different values of dust optical depth. The equivalent width of the CO_2 band is calculated for appropriate geometrical condition of orbit 1639 orbit using EMCD model. We over plot the measured equivalent width obtained from SPICAM IR spectra integrated from 1420 nm to 1461 nm. The comparison of data set with curves of growth for different τ

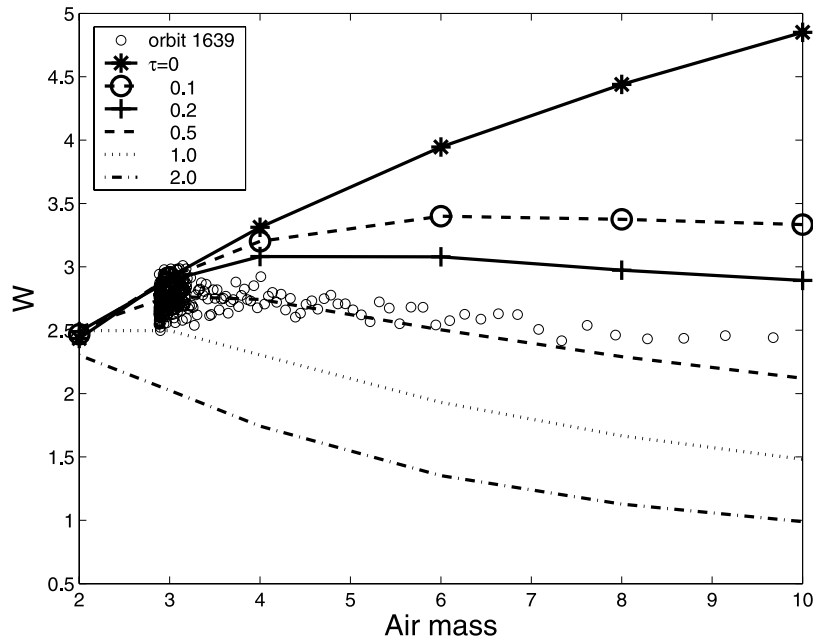


Figure 12. Equivalent width of CO₂ band at 1.43–1.45 μm as a function of the air mass calculated for different dust optical depths (lines). Circles are equivalent widths of the same CO₂ band from SPICAM spectra measured on the orbit 1639 (spot pointing observation). Estimated dust optical depth τ equals 0.4–0.5.

indicates the value of $\tau \sim 0.4$ – 0.5 . Such a value of dust optical depth for air mass > 5 results in underestimation of H₂O abundance in two times (Figure 11). We therefore restrict our results to observation with emission and solar zenith angles $< 60^\circ$. Still, the influence of dust and clouds is possible.

[68] We estimate the effect of the aerosol on the 1.38 μm band for a typical nadir observation with solar zenith angle 60° and observation angle 0° . We chose the dust model described above and water ice cloud model with $g = 0.63$ and $\omega_0 = 0.99$ [Clancy *et al.*, 2003]. The optical depth of dust varies from 0.1 in the aphelion season to >1 in the perihelion dust storm season. The cloud optical depth reaches 0.15 in the aphelion cloud belt [Smith, 2004]. In the near IR the optical depth is 1.5–3 times higher than that measured in the IR thermal range [Clancy *et al.*, 2003].

[69] We computed equivalent widths of water vapor 1.38-μm band for H₂O abundance of 20 pr μm, and several values of dust and clouds optical depths. Two aerosol distributions were considered: an uniformly mixed one, and an aerosol layer imitating a cloud at the altitude of 20–22 km. We tested three variants of H₂O vertical distribution: (1) without saturation, (2) well mixed up to 20 km, and (3) well mixed up to 10 km (Figure 13). The effect of dust on the equivalent width is weak for $\tau < 1$. The case of $\tau = 1$ and H₂O confined below 10 km is not realistic because such distribution is typical for aphelion season, and a clean atmosphere. For other cases the effect of dust is not higher than 20%. During a dust storm the vertical extension of dust is large, and expected influence is much stronger. In the aphelion ($L_s = 0^\circ$ – 150°) the cloud activity is maximal. H₂O saturates above 10–20 km and water ice clouds overlay a water-rich atmosphere. With the optical thickness of clouds

of $\tau = 0.3$ – 0.4 [Clancy *et al.*, 2003] the underestimation of water vapor is significant: 40–50%.

[70] Further information about dust loading during Mars Express observation from PFS could help us to correct our data for dust and cloud scattering.

7.4. A Possible Instrumental Effect

[71] The observed depth of the CO₂ band in our spectra is systematically lower as compared with synthetic models calculated, using EMCD atmospheric data. The estimation of surface pressure gives 0.8–1.0 mbar lower values than EMCD pressures. There might be different ways to explain this difference, with a stray light in the system (8–10% of a stray light is needed), or underestimated far side lobes of the instrumental function of the spectrometer. These possibilities are discussed in detail by Korablev *et al.* [2006, section 3]. Either instrumental effect decreases the depth of the H₂O band in synthetic model by 0.3–0.5%, and the retrieved H₂O abundance is increased by 40% on the average.

[72] Summarizing, the decrease of retrieved H₂O abundance due to new spectroscopic database which is about 20–25% is on average compensated by the influence of dust and clouds, presently ignored, except for more significant effect during dust storm and cloud seasons. The suspected instrumental effects could further increase the retrieved water abundance up to 40%. Other systematic uncertainties are much less important, the most noticeable in an additive uncertainty of about ± 2 – 3 pr μm due to imperfect solar spectrum.

8. Conclusions

[73] In this paper we present the H₂O distribution in Martian atmosphere obtained during MY 27 with SPICAM

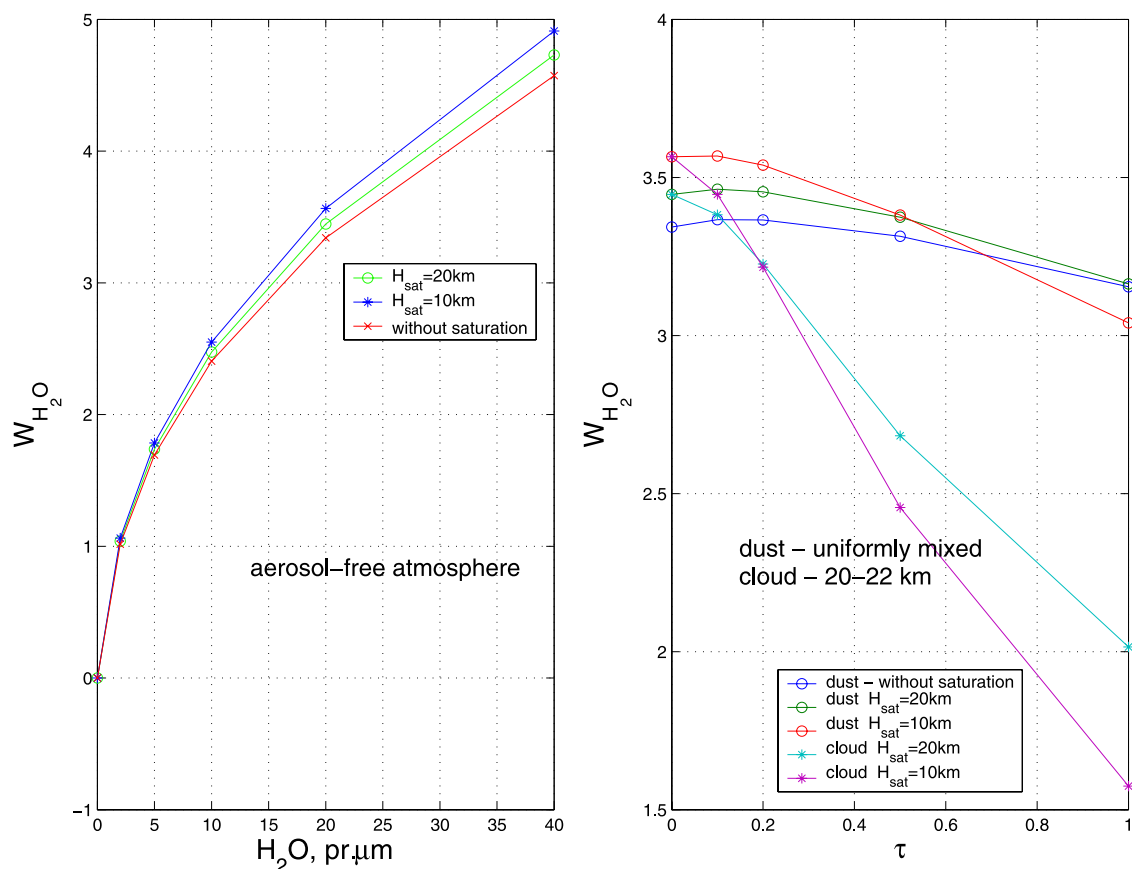


Figure 13. (left) Dependence of equivalent width of the H₂O band on the H₂O abundance for different vertical distribution of water vapor: uniformly mixed up to 100 km, uniformly mixed up to 20 km, and uniformly mixed up to 10 km. (right) Dependence of equivalent width of the H₂O band on the aerosol optical depth for a fixed H₂O abundance of 20 pr μm and two aerosol models: uniformly mixed dust and cloud at the altitude of 20–22 km. The same vertical distributions of water vapor are considered.

IR spectrometer on Mars Express. The AOTF spectrometer is a compact and light-weight instrument with good spectral resolution and high signal-to-noise ratio. It is a candidate instrument to measure water vapor in future Mars missions. After a proper validation the data are statistically very accurate.

[74] From SPICAM IR measurements we obtained the seasonal distribution of water vapor and geographic distributions for selected seasons, and compared our data set with previous observations to explore possible interannual variability of the Martian water cycle. Compared to TES and MAWD results, our measurements indicate systematically lower water abundance for both hemispheres. The difference is as high as a factor of 1.8–2 compared to TES, and a factor of 1.5–1.7 compared to MAWD results. In turn, our measurements are very close to Mars Express OMEGA results for the north pole: 50–55 pr μm for north pole maximum, while at low and middle latitudes OMEGA results are closer to TES and MAWD. In the southern hemisphere, the observed south pole maximum and seasonal distribution of water vapor during is closer to TES rather than to MAWD. The retrieved absolute values are still lower, but the maximum occurs at $L_s = 290^\circ\text{--}310^\circ$, in accordance with TES results, and the spatial distribution of water vapor at $L_s = 285^\circ\text{--}305^\circ$ resem-

bles the MY24 TES measurements. During this year relatively clear dust conditions were reported at perihelion. For the moment a systematic aerosol measurements on from Mars Express are not available. We hope that aerosol measurements by other Mars Express experiments will help to understand the noted disagreements, in particular the difference between SPICAM and MAWD H₂O abundances retrieved from the same spectral band.

[75] We analyzed the possible sources of uncertainties of the water vapor retrieval. The effect of aerosol scattering is discussed. We estimate that the effect of dust is minor for air mass below ~ 3.5 , and we limited our data set to air mass < 4 . The influence of clouds is more important, and H₂O can be largely underestimated in the aphelion cloud belt season. The recent HITRAN 2004 spectroscopic database contains two times more H₂O lines in 1.37- μm range comparing to HITRAN 2000. The use of this database results in higher water absorption for same gas amount (lower retrieved values). The expected decrease of H₂O abundance derived from our spectra with HITRAN 2004 is estimated as 20–25%. In this context, a revision of MAWD data can be envisaged.

[76] We plan to continue the study of water vapor from SPICAM measurements using a larger data set and recent

spectroscopic database. Using data of other Mars Express instruments continue validation of our data, and we will correct for the aerosol scattering.

[77] Mars climate is now being extensively studied by different experimental methods. Advancing from occasional measurements to quasi continuous monitoring we are coming to situation when the same climate parameter is simultaneously measured by different instruments using different techniques. This situation, typical for earth observation, requires intercomparison and validation. Mars Express, where three instruments measure remotely the H₂O abundance is an excellent opportunity for such studies. We believe that combined measurements of water vapor by different Mars Express experiments will help to improve our understanding of Mars water cycle.

[78] **Acknowledgments.** We thank our colleagues N. Ignatiev at IKI and E. Lellouch and T. Fouchet at Meudon for information about new line parameters and useful discussion for retrieval methods and M. Smith at NASA Goddard Space Flight Center for the cooperation for comparison of data set. We are grateful to ISSI for organizing a team on comparison of Mars water data sets, and we thank all the members of the team for helpful discussion. The authors would like to thank our reviewers for careful revision and useful comments that helped to improve this manuscript. We thank our collaborators at the three institutes for the design and the fabrication of the instruments (Service d'Aeronomie/France, BIRA/Belgium and IKI/Moscow). The Russian team thanks a RFBR grant 04-02-16856a for finance support. A. Fedorova was supported by grant MK-1287.2006.2. We wish to thank Russian Academy of Sciences, Roskosmos, CNRS and CNES for financing SPICAM in France. We are grateful to J.-Y. Chaufray, S. Guilbert, and E. Villard at Service d'Aeronomie for the help with SPICAM IR calibration and A. Stepanov for design of spectrometer. We also acknowledge E. Dimarellis, A. Reberac and M. Barthelemy at Service d'Aeronomie for handling routine operations of the SPICAM instruments.

References

- Barker, E. S. (1976), Martian atmospheric water observations: 1972–74 apparition, *Icarus*, **28**, 247–268.
- Barker, E. S., R. A. Schorn, A. Worszczyk, R. G. Tull, and S. J. Little (1970), Mars: Detection of atmospheric water vapor during the southern hemisphere spring and summer season, *Science*, **170**, 1308–1310.
- Basilevsky, A. T., et al. (2006), Search for the cause of anomalous low epithermal neutron flux near Terre Arabia, Mars, *Sol. Syst. Res.*, in press.
- Bibring, J.-P., et al. (2004), OMEGA: Observatoire pour la Mineralogie, l'Eau, les Galces et l'Activite, *Eur. Space Agency Spec. Publ., ESA-SP 1240*, 37–50.
- Clancy, R. T., A. W. Grossman, and D. O. Muhleman (1992), Mapping Mars water vapor with the very large array, *Icarus*, **100**, 48–59.
- Clancy, R. T., A. W. Grossman, M. J. Wolff, P. B. James, D. J. Rudy, Y. N. Billawala, B. J. Sandor, S. W. Lee, and D. O. Muhleman (1996), Water vapor saturation at low altitudes around Mars Aphelion: A key to Mars climate?, *Icarus*, **122**, 36–62.
- Clancy, R. T., M. J. Wolff, and P. R. Christensen (2003), Mars aerosol studies with the MGS TES emission phase function observations: Optical depths, particle sizes, and ice cloud types versus latitude and solar longitude, *J. Geophys. Res.*, **108**(E9), 5098, doi:10.1029/2003JE002058.
- Conrath, B., R. Curran, R. Hanel, V. Kunde, W. Maguire, J. Pearl, J. Pirraglia, and J. Welker (1973), Atmospheric and surface properties of Mars obtained by infrared spectroscopy on Mariner 9, *J. Geophys. Res.*, **78**, 4267–4278.
- Davies, D. W. (1979), The vertical distribution of Mars water vapor, *J. Geophys. Res.*, **84**, 2875–2879.
- Davies, D. W., and L. A. Wainio (1981), Measurements of water vapor in Mars' Antarctic, *Icarus*, **45**, 216–230.
- Durry, G., V. Zeninari, B. Parvitte, T. Le Barbu, F. Lefevre, J. Ovarlez, and R. R. Gamache (2005), Pressure-broadening coefficients and line strengths of H₂O near 1.39 μm : Application to the in situ sensing of the middle atmosphere with balloonborne diode lasers, *J. Quant. Spectrosc. Radiat. Transfer*, **94**, 387–403.
- Encenaz, T., et al. (2005a), A mapping of Martian water sublimation during early northern summer using OMEGA/Mars Express, *Astron. Astrophys.*, **441**, L9–L12.
- Encenaz, T., et al. (2005b), Infrared imaging spectroscopy of Mars: H₂O mapping and determination of CO₂ isotopic ratios, *Icarus*, **179**, 43–54.
- Evans, K. F. (1998), The spherical harmonics discrete ordinate method for three-dimensional atmospheric radiative transfer, *J. Atmos. Sci.*, **55**, 429–446.
- Farmer, C. B., and D. D. LaPorte (1972), The detection and mapping of water vapor in the Martian atmosphere, *Icarus*, **16**, 34–46.
- Farmer, C. B., D. W. Davies, A. L. Holland, D. D. LaPorte, and P. E. Doms (1977), Mars: Water vapor observations from the Viking orbiters, *J. Geophys. Res.*, **82**, 4225–4248.
- Fedorova, A. A., A. V. Rodin, and I. V. Baklanova (2004), MAWD observations revisited: Seasonal behavior of water vapor in the Martian atmosphere, *Icarus*, **171**, 54–67.
- Feldman, W. C., et al. (2004), Global distribution of near-surface hydrogen on Mars, *J. Geophys. Res.*, **109**, E09006, doi:10.1029/2003JE002160.
- Feldman, W. C., et al. (2005), Topographic control of hydrogen deposits at low latitudes to midlatitudes of Mars, *J. Geophys. Res.*, **110**, E11009, doi:10.1029/2005JE002452.
- Fiorenza, C., and V. Formisano (2005), A solar spectrum for PFS data analysis, *Planet. Space Sci.*, **53**, 1009–1016.
- Forget, F., F. Hourdin, R. Fournier, C. Hourdin, O. Talagrand, M. Collins, S. R. Lewis, P. L. Read, and J.-P. Huot (1999), Improved general circulation models of the Martian atmosphere from the surface to above 80 km, *J. Geophys. Res.*, **104**, 24,155–24,176.
- Formisano, V., et al. (2005), The planetary Fourier spectrometer (PFS) onboard the European Mars Express mission, *Planet. Space Sci.*, **53**, 963–974.
- Gamache, R. R., S. P. Neshyba, J. J. Planeaux, A. Barbe, L. Regalia, and J. B. Pollack (1995), CO₂-broadening of water vapor lines, *J. Mol. Spectrosc.*, **170**, 131–151.
- Gurwell, M. A., et al. (2000), Submillimeter wave astronomy satellite observations of the Martian atmosphere: Temperature and vertical distribution of water vapor, *Astrophys. J.*, **539**, L143–L146.
- Hanel, R., et al. (1972), Investigation of the Martian environment by infrared spectroscopy on Mariner 9(A 5. 2), *Icarus*, **17**, 423.
- Howard, T. N., D. E. Burch, and D. Williams (1956), Infrared transmission of synthetic atmosphere, *J. Opt. Soc. Am.*, **46**, 186–190, 237–245, 334–338, 442–445.
- Hunten, D. M., A. L. Sprague, and L. R. Doose (2000), Correction for dust opacity of Martian atmospheric water vapor abundances, *Icarus*, **147**, 42–48.
- Ignatiev, N. I., L. V. Zasova, V. Formisano, D. Grassi, and A. Maturilli (2002), Water vapor abundance in Martian atmosphere from revised Mariner 9 IRIS data, *Adv. Space Rev.*, **29**, 157–162.
- Jakosky, B. M., and C. B. Farmer (1982), The seasonal and global behavior of water vapor in Mars atmosphere: Complete global results of the Viking atmospheric water detector experiment, *J. Geophys. Res.*, **87**, 2999–3019.
- Jakosky, B. M., R. W. Zurek, and M. R. La Pointe (1988), The observed day-to-day variability of Mars atmospheric water vapor, *Icarus*, **73**, 80–90.
- Korablev, O., et al. (2006), SPICAM IR acousto-optic spectrometer experiment on Mars Express, *J. Geophys. Res.*, **111**, E09S03, doi:10.1029/2006JE002696.
- Kurucz, R. (1995), The solar spectrum: Atlases and line identifications, in *Workshop on Laboratory and Astronomical High Resolution Spectra*, *Astron. Soc. Pac. Conf. Ser.*, vol. 81, edited by A. J. Saival, R. Blomme, and N. Grevesse, p. 17, Astron. Soc. of the Pac., San Francisco, Calif.
- Liu, J., M. I. Richardson, and R. J. Wilson (2003), An assessment of the global, seasonal, and interannual spacecraft record of Martian climate in the thermal infrared, *J. Geophys. Res.*, **108**(E8), 5089, doi:10.1029/2002JE001921.
- Martin, T. Z., and M. I. Richardson (1993), New dust opacity mapping from Viking infrared thermal mapping data, *J. Geophys. Res.*, **98**, 10,941–10,949.
- Matveev, V. S. (1972), Approximate representations of absorption coefficient and equivalent widths of lines with Voigt profile, *J. Appl. Spectrosc.*, **16**, 168–172.
- Mitrofanov, I., et al. (2002), Maps of subsurface hydrogen from the high energy neutron detector, Mars Odyssey, *Science*, **297**, 78–81.
- Montmessin, F., F. Forget, P. Rannou, M. Cabane, and R. M. Haberle (2004), Origin and role of water ice clouds in the Martian water cycle as inferred from a general circulation model, *J. Geophys. Res.*, **109**, E10004, doi:10.1029/2004JE002284.
- Moroz, V. I., and A. E. Nadzhip (1975), Preliminary measurement results of the water vapor content in the planetary atmosphere from measurements onboard the Mars 5 spacecraft, *Cosmic Res., Engl. Transl.*, **13**, 28–30.
- Moroz, V. I., and A. E. Nadzhip (1976), Water vapor in the atmosphere of Mars based on measurements on board Mars 3, *Cosmic Res., Engl. Transl.*, **13**, 658–670.
- Ockert-Bell, M. E., J. F. Bell III, J. B. Pollack, C. P. McKay, and F. Forget (1997), Absorption and scattering properties of the Martian dust in the solar wavelengths, *J. Geophys. Res.*, **102**, 9039–9050.

- Parvitte, B., V. Zeninari, I. Pouchet, and G. Durry (2002), Diode laser spectroscopy of H₂O in the 7161–7185 cm⁻¹ range for atmospheric applications, *J. Quant. Spectrosc. Radiat. Transfer*, *75*, 493–505.
- Pollack, J. B., et al. (1993), Near-infrared light from Venus' nightside—A spectroscopic analysis, *Icarus*, *103*, 1–42.
- Richardson, M. I., and R. J. Wilson (2002), Investigation of the nature and stability of the Martian seasonal water cycle with a general circulation model, *J. Geophys. Res.*, *107*(E5), 5031, doi:10.1029/2001JE001536.
- Rizk, B., W. K. Wells, D. M. Hunten, C. R. Stoker, R. S. Freedman, T. Roush, J. B. Pollack, and R. M. Haberle (1991), Meridional Martian water abundance profiles during the 1988–1989 season, *Icarus*, *90*, 205–213.
- Rodin, A. V., O. I. Korablev, and V. I. Moroz (1997), Vertical distribution of water in the near-equatorial troposphere of Mars: Water vapor and clouds, *Icarus*, *125*, 212–229.
- Rothman, L. S., et al. (2003), The HITRAN molecular spectroscopic database: Edition of 2000 including through 2001, *J. Quant. Spectrosc. Radiat. Transfer*, *82*, 5–44.
- Rothman, L. S., et al. (2005), The HITRAN 2004 Molecular Spectroscopic Database, *J. Quant. Spectrosc. Radiat. Transfer*, *96*, 139–204.
- Smith, M. D. (2002), The annual cycle of water vapor on Mars as observed by the Thermal Emission Spectrometer, *J. Geophys. Res.*, *107*(E11), 5115, doi:10.1029/2001JE001522.
- Smith, M. D. (2004), Interannual variability in TES atmospheric observations of Mars during 1999–2003, *Icarus*, *167*, 148–165.
- Smith, M. D., M. J. Wolff, R. T. Clancy, N. Spanovich, D. Banfield, A. Ghosh, and in the Athena Science Team (2006), Mars exploration rovers MINI-TES observations of boundary layer temperatures and aerosol optical depth, in *Second Workshop on Mars Atmosphere Modelling and Observations, Granada, Spain*, edited by F. Forget et al., p. 133, Lab. de Météorol. Dyn., Paris.
- Spinrad, H., G. Munch, and L. D. Kaplan (1963), The detection of water vapor on Mars, *Astrophys. J.*, *137*, 1319–1321.
- Sprague, A. L., D. M. Hunten, R. E. Hill, B. Rizk, and W. K. Wells (1996), Martian water vapor, 1988–1995, *J. Geophys. Res.*, *101*, E10, 23,229–23,241.
- Sprague, A. L., D. M. Hunten, R. E. Hill, L. R. Doose, and B. Rizk (2001), Water vapor abundances over Mars north high latitude regions: 1996–1999, *Icarus*, *154*, 183–189.
- Sprague, A. L., D. M. Hunten, R. E. Hill, L. R. Doose, and R. E. Hill (2003), Mars atmospheric water vapor abundance: 1996–1997, *Icarus*, *163*, 88–101.
- Sprague, A. L., D. M. Hunten, L. R. Doose, R. E. Hill, W. V. Boynton, M. D. Smith, and J. C. Pearl (2006), Mars atmospheric water vapor abundance: 1991–1999, emphasis 1998–1999, *Icarus*, in press.
- Thuillier, G., et al. (2003), The solar spectral irradiance from 200 to 2400 nm as measured by the SOLSPEC spectrometer from the Atlas and Eureca mission, *Sol. Phys.*, *62*, 1233–1250.
- Titov, D. V., W. J. Markiewicz, N. Thomas, H. U. Keller, R. M. Sablotny, M. G. Tomasko, M. T. Lemmon, and P. H. Smith (1999), Measurements of the atmospheric water vapor on Mars by the Imager for Mars Pathfinder, *J. Geophys. Res.*, *104*, 9019–9026.
- Zasova, L., et al. (2005), Water clouds and dust aerosols observations with PFS MEX at Mars, *Planet. Space Sci.*, *53*, 1065–1077.

J.-L. Bertaux and S. Perrier, Service d'Aéronomie, CNRS, BP 3, F-91371 Verrières-le-Buisson, France.

A. Fedorova, A. Kiselev, and O. Korablev, IKI, 84/32 Profsoyuznaya, 117997 Moscow, Russia. (fedorova@spectrum.iki.rssi.ru)

A. Rodin, Moscow Institute of Physics and Technology, Institutsky dr. 9, 141700 Dolgoprudnyi, Russia.